Trends in advanced sciences and technology

Trends in Advanced Sciences and Technology

Volume 1 Article 11

2024

Dynamic analysis and experimental verification of flexible unbalance rotor supported by two identical journal bearings

Omar Ahmed
Department of Mechanical Design, Faculty of Engineering, Mataria, Helwan University, P.O. Box 11718, Helmeiat-Elzaton, Cairo, Egypt

Hussein Sayed
Department of Mechanical Design, Faculty of Engineering, Mataria, Helwan University, P.O. Box 11718, Helmeiat-Elzaton, Cairo, Egypt

T.A. El-Sayed
Department of Mechanical Design, Faculty of Engineering, Mataria, Helwan University, P.O. Box 11718, Helmeiat-Elzaton, Cairo, Egypt, tamer_alsayed@m-eng.helwan.edu.eg

How to Cite This Article

Ahmed, Omar; Sayed, Hussein; and El-Sayed, T.A. (2024) "Dynamic analysis and experimental verification of flexible unbalance rotor supported by two identical journal bearings," *Trends in advanced sciences and technology*: Vol. 1, Article 11.
DOI: 10.62537/2974-444X.1011
Available at: https://tast.researchcommons.org/journal/vol1/iss1/11

ORIGINAL STUDY

Dynamic Analysis and Experimental Verification of Flexible Unbalanced Rotors Supported by Two Identical Journal Bearings

Omar Ahmed [a], Hussein Sayed [a], Tamer Ahmed El-Sayed [a,b,*]

[a] Department of Mechanical Design, Faculty of Engineering, Mataria, Helwan University, Egypt
[b] School of Engineering, UH Hosted by Global Academic Foundation, Cairo, Egypt

Abstract

Background: **Analyzing the vibrations for rotor-bearing systems is a critical issue in the field of rotor dynamics. It is crucial to identify rotary machine vibrations, behaviors, and stability conditions. The main causes of vibration in rotating machinery are unbalanced masses, misalignment, mechanical looseness, shaft cracks, and other defects.**

Methods: **This paper investigates the experimental verification of a theoretical model, using a steel shaft with a disc set at the midpoint, supported by two symmetric fluid film bearings. The study examines the effect of unbalance on the dynamic behavior of the rotor and its vibration characteristics. The experimental investigation involved setting up a test rig, installing the journal bearing and rotor, and measuring relevant parameters. The theoretical analysis employed the solution of the Reynolds equation to determine the bearing coefficients, which were then modeled as a function of the Sommerfeld number using a polynomial fit. A finite element model with a consistent matrix formulation was used to simulate the shaft, including the external load and four degrees of freedom per node.**

Results: **The theoretical model was validated against experimental results in both the time and frequency domains, considering the effect of unbalanced masses. The results are presented using orbit plots, system responses, and fast fourier transform (FFT) spectra. The vibration analysis results show the whirl phenomena before it becomes uncontrollable and leads to self-excited vibration.**

Conclusions: **The theoretical model based on nonlinear analysis was in agreement with the experimental analysis for all rotational speed ranges. The resonant speeds of 5107 rpm and 5850 rpm were observed in both the theoretical and experimental studies, respectively. However, a noticeable discrepancy was observed when the speed exceeded the threshold speed in both the first and second-order theoretical analyses.**

Keywords: Finite-element model, Hydrodynamic bearing forces, Linear and nonlinear analysis, Nonlinear-bearing coefficients, Rotor dynamic model

1. Introduction

High-speed pumps, turbines, hydraulic turbochargers, machine tools, and automobiles are some of the industrial applications that use rotor-bearing systems with high rotating speeds. Research has identified excessive vibration and instability as fundamental challenges in the rotor dynamics of such turbomachinery. Furthermore, these studies emphasize the critical role of varying rotor speeds in influencing rotor-bearing behavior and performance (Mourelatos, 2001; San Andrés, 2006; El-Sayed and Farghaly, 2016; El-Sayed and Fatah, 2016). The vibration and stability of rotor-bearing systems affect the performance of machinery and equipment. As the rotational speed and load increase, it becomes more important to reduce vibration in a rotor-bearing system. For example, unbalance and instability of the rotor can cause excessive wear and even catastrophic failures. Therefore, it is essential to

---

Received 25 April 2024; revised 30 May 2024; accepted 3 June 2024.

* Corresponding author at: Department of Mechanical Design, Faculty of Engineering, Mataria, Helwan University, PO Box 11718, Helmeiat-Elzaton, Cairo, Egypt.
E-mail address: tamer_alsayed@m-eng.helwan.edu.eg (T.A. El-Sayed).

https://doi.org/10.62537/2974-444X.1011

Nomenclature

Symbol	*Definition*
C_{ab}, C_{abc}	Dimensionless bearing damping coefficients in (X-Y) coordinates: where, a, b, c = X, Y
K_{ab}, K_{abc}	Dimensionless bearing stiffness coefficients in (X-Y) coordinates: a, b, c = X, Y
F_x, F_y	Bearing forces (N)
[M]	Mass matrix of the element
P_0	Dimensionless steady-state pressure
$P_X, P_Y, P_{X'}, P_{Y'}, P_{XX}, P_{XY}$ $P_{YY}, P_{X'Y}, P_{Y'X}, P_{XX'}, P_{YY'}$	Gradient pressure in X-Y coordinate
X_j, Y_j, X_d, Y_d	Transverse motion of journal and disk
θ_x θ_y	Rotations affected by bending deformation
[G]	Gyroscopic matrix
[K]	Stiffness matrix of the element
c	Radial Clearance
H	Dimensionless fluid film thickness. $H = \frac{h}{c}$
h	Fluid film thickness (m)
L	Length of fluid film bearing (m)
P	Dimensionless pressure of the fluid film $P = \frac{p}{6\mu\Omega}\left(\frac{c}{R}\right)^2$
p	The pressure of fluid film (N/m^2)
R	Radius of the journal bearing. (m)
W_b	The bearing load (N)
$X, \dot{X}, \ddot{X}$	Dimensionless displacement, velocity, and acceleration in Cartesian coordinates
Z	Shaft coordinate in axial direction
ε	Eccentricity ratio. $\varepsilon = \frac{e}{c}$
μ	Viscosity of the fluid (Ns/m^2)
ρ	Density of the fluid (kg/m^3)
Ω	Shaft speed

ensure stability and minimize vibration for the performance, efficiency, and structural integrity of these rotating machines. High-speed rotors pose several challenges for design and operation, such as rotor balancing, which is necessary to reduce unbalanced forces and moments that can cause vibration, ensuring mechanical stability and integrity, and addressing vibration issues. Material selection, lubrication systems, and advanced engineering techniques are used to overcome these challenges and ensure the safe and efficient operation of high-speed rotors. Vibration analysis and modes for rotors involve studying the natural frequencies and mode shapes of the rotor system. This information is vital for understanding how the rotor responds to external forces. Moreover, managing rotor vibration is a critical aspect of rotor-bearing system reliability. By identifying the root causes, implementing appropriate mitigation measures, monitoring vibration levels over time, and using fast fourier transform (FFT) spectrum analysis. Unbalanced rotors can cause harmful vibrations in rotating machinery, which has been extensively investigated by both theoretical and experimental research in the past decades. Several reviews have summarized the literature on this topic (Flack and Rooke, 1980; Hashimoto and Wada, 1990; Gupta et al., 1993; Xu and Marangoni, 1994; Zhao et al., 1994; De Rosa and Rossi, 1996; Lee and Van Moorhem, 1996; Kreuzinger-Janik and Irretier, 2000).

1.1. *Analysis of stability and dynamic behavior in unbalanced rotor-bearing systems*

To study the instability and behavior of rotor-bearing systems, two research methods are commonly used. One is to perform experimental studies, either in a laboratory setting or in real industrial applications (Al Yahyai and Mba, 2014). The other is to use mathematical models and analytical analysis, based on the system's equation of motion, to identify the features of rotor-bearing systems (Braut et al., 2008; Shen et al., 2008; Zhang et al., 2009; Meybodi et al., 2012; Taplak and Parlak, 2012; Zanarini and Cavallini, 2012; Jalali et al., 2014; Özer et al., 2015; Perez and Rodríguez, 2021). Adiletta et al. (1997) conducted a study on the nonlinear behavior of an unbalanced rigid rotor, which was supported by two symmetrical plain journal bearings. This study is divided into parts: the first part involves theoretical analysis, and the other part involves experimental verification of theoretical results. The comparison pointed out that the experimental results and the theoretical model analysis agreed well. Sinha et al. (2004) proposed a method to estimate the rotor unbalance and misalignment during operation. They verified the method using an experimental setup. Driot et al. (2006) studied the dynamic behavior of a flexible rotor system theoretically and verified their results experimentally. The numerical and analytical model results are favorably compared with the experimental results. Balducchi et al. (2014) demonstrated an experimental study on an unbalanced rigid rotor of Pelton turbines supported by two identical aerodynamic foil bearings. The study presents the nonlinear behavior of the rotor, synchronous, and subsynchronous vibrations, and depicts the waterfall diagrams. The experimental results are compared with very simplified theoretical predictions based on certain assumptions and showed a good agreement. Zhu et al. (2020) used a finite-element method based on the Timoshenko beam element to study the dynamic analysis of a flexible rotor supported by ball bearings, considering the influences of unbalanced force, nonlinear-bearing force, and rotor gravity. The comparison between theoretical and experimental results showed a small percentage of error of less than 10%. Parmar et al. (2020) studied the effect of unbalance on a rotor supported by two self-align ball bearings. They established a mathematical model to predict the nonlinear behavior of the rotor under different shaft speeds. They observed that the shaft rotational speed and radial load have a significant effect on the system's periodicity. They validate the simulated results of the analytical model with an experimental test-rig setup. Li et al. (2021) demonstrated a rotor-bearing system involving multidisk bolted joints. These joints are subjected to moments and unbalanced forces during operation. They used bifurcation diagrams and trajectory plots to study the rotor's stability and vibration characteristics. Finally, they used experimental rotor dynamic responses to verify their theoretical results. Briend et al. (2021) focused on studying the effect of mass and unbalanced forces on parametric rotor instability and dynamic behavior. The analysis of the predicted results was achieved in terms of shaft trajectories and FFT spectrums, and permitted experimental validation for the mathematical model.

Miraskari et al. (2018a) and Miraskari et al. (2018b) modeled bearing forces with linear and nonlinear-bearing dynamic coefficients to investigate the flexible rotor instability. They predicted bifurcation and orbit plots for speeds below and above threshold speed. In addition, they used the expiremental results of Wang and Khonsari (2006). Huang et al. (2022) utilized a novel double-layer flexible support tilting pad bearing to reduce the undesired vibrations of the rotor-bearing system and improve the stability. Experiments were carried out to investigate the vibration characteristics of the rotor. The results proved that double-layer flexible support tilting pad bearing is excellent in vibration attenuation. Wang et al. (2022) studied the effect of unbalaced orientation turbochargers installed on automobile engines. The results demonstrate that the vibration characteristics are significantly influenced by the unbalanced orientation. To reduce dynamical variations between turbochargers of the same kind and to provide a high-efficiency turbocharger with low vibration and noise, it is suggested to keep the unbalanced orientation in the range of 0–60°. Yin et al. (2021) conducted a nonlinear analysis to study the instability and dynamic characteristics of an unbalanced rotor supported by aerostatic journal bearings. It is demonstrated that the rotor mass has a significant impact on the dynamic responses of the rotor. The findings are useful for designers in creating aerostatic bearing rotor systems with the required operating speed and stability. El-Sayed and Sayed (2022), El-Sayed and Farghaly (2016), El-Sayed et al. (2023), Elsayed et al. (2023), Sayed and El-Sayed (2022a, 2022b), and Sayed et al. (2023) focused on studying the instability and bifurcation plots for a jeffcott rotor supported by two identical journal bearings. The results proved that third-order bearing coefficients are effectively used in the rich dynamics of rotor-bearing systems.

1.2. Bearing dynamic coefficient calculations

Elsayed et al. (2023) calculated the bearing coefficients based on first-order and second-order analyses for an inclined pad hydrodynamic thrust bearing using the finite-difference method in polar coordinates. The results showed the effect of changing misalignment angle, shaft rotational speed, and film thickness on the dynamic coefficients. Ahmed et al. (2023) established a method for analyzing the behavior of an elastic rotor supported by two symmetrical hydrodynamic journal bearings. The bearing coefficients based on second-order analysis were calculated using the small perturbation approach, and the shaft was simulated using a finite-element model with a consistent matrix formulation. Tofighi-Niaki and Safizadeh (2023) proposed a turbo-dynamic model of the rotor-bearing system to assess the effect of wear and instability on rotor behavior. The results showed that the thermal and dynamic conditions affect the dynamic characteristics of the rotor. Katinić et al. (2023) analyzed the dynamic behavior of a rotor-bearing system with two symmetrical disks located between the plain bearings. They studied the effect of gyroscopic mass on the natural frequencies of the system. Kartheek et al. (2023) analyzed the responses of a flexible shaft with three disks supported on hydrodynamic journal bearings. They developed Campbell plots to identify the shaft's critical speeds. They also verified the analytical analysis using an experimental test rig. Lu et al. (2023) investigated the influence of eccentricity and bearing clearance on the rotor-bearing system's dynamic performance. They concluded that bearing clearance and eccentricity affect the nonlinear-bearing forces of the system, which in turn cause the system to exhibit rich and complex dynamic behaviors. Mutra and Srinivas (2022) developed a comprehensive mathematical model for a turbocharger rotor system. Their model incorporates the complexities of a nonuniform, flexible, stepped turbo-compressor shaft supported by floating ring bearings. This model facilitated dynamic analysis and optimization of the rotor system, aiming to enhance its performance and durability under exhaust emission loads. The study also investigated critical vibration characteristics and addressed common failure modes such as bearing wear, impeller-casing rubs, and shaft cracks. In a subsequent work, Mutra and Srinivas (2020) presented an efficient methodology to predict reliable stiffness and damping parameters for floating ring bearings supporting a dual disk rotor system. This method achieved accurate results with minimal computational effort and algorithmic complexity. Their findings demonstrate the effectiveness of the optimization-based approach in improving the understanding and optimization of cylindrical floating ring journal bearings used in automotive turbochargers. Finally, Mutra and Srinivas (2021) conducted a comprehensive hydrodynamic analysis of a high-speed turbocharger rotor-bearing system with floating ring bearings, focusing on transient operating conditions. Their analysis considered temperature-dependent lubricant viscosity and film clearances to calculate pressure distributions and dynamic bearing forces. This approach allowed for a deeper understanding of the system's dynamic behavior and stability issues during critical start-up and shut-down phases. The study highlights the importance of incorporating temperature-dependent viscosity and film clearances for accurate dynamic analysis of turbocharger rotor-bearing systems.

1.3. Key objectives and novel contributions of the paper

This paper presents an analytical model of a flexible rotor supported by two symmetrical journal bearings, using the finite-element method based on the Euler Bernoulli beam theory. The equations of motion are derived from Hamilton's principle and solved numerically. The theoretical analysis is validated experimentally for both time and frequency domains, as well as orbit plots. Furthermore, a simple study is conducted to discuss the effect of unbalanced masses and changes in shaft rotational speeds on the nonlinear response and behavior of the rotor. Previous research highlights the significance of analyzing rotor dynamics supported by journal bearings using bearing coefficients. Some studies have employed these issues using linear bearing coefficients, while others incorporated both linear and nonlinear models. However, a key limitation of this approach is the variability of bearing coefficients with the applied static load and the bearing parameters. The novelty of this paper is in solving this drawback by introducing a technique based on polynomial fitting. This enables the investigation of the stability of a rotor supported by two journal bearings using orbit plots and bifurcation diagrams. The paper is organized as follows: Section 2 introduces the theoretical model and the equations of motion of the rotor system. Section 3 describes the experimental setup and the test rig used to obtain the experimental data. Section 4 compares the numerical results with the experimental signals and discusses the main findings. Section 5 summarizes the main conclusions and contributions of this paper.

1.4. Theoretical model and equation of motion

The system equation for the rotor-bearing system shown in Fig. 1a, b is derived through mathematical analysis utilizing the finite-element model. Fig. 2 illustrates a model of a rotating shaft, which comprises four elements. Each element is defined by two nodes located at their respective ends. The shaft possesses a straight configuration, uniform properties, and a round cross-section. Each element has two nodes, leading to a total of eight degrees of freedom per element. Both transverse motion and rotation around the x and y-axes are permitted at each node.

The system displacement vector is $X = [\mathrm{x}_1\ \mathrm{y}_1\ \theta_{x1}\ \theta_{y1}\ \mathrm{x}_2\ \mathrm{y}_2\ \theta_{x2}\ \theta_{y2}]$.

1.5. System equation of motion

By utilizing Hamilton's principle, the kinetic and potential energy of each element can be defined in matrix form using its nodal variables. This approach allows the formulation of the system's equation of motion using the finite-element method:

$$\int_{t1}^{t2} (\delta \mathrm{N} - \delta \mathrm{P} + \delta \mathrm{W})\mathrm{dt} = 0 \tag{1}$$

In this context, N denotes the kinetic energy, while P stands for the potential energy, and W signifies the work performed by external nodal forces (NP). After formulating the kinetic energy, elastic strain potential energy, and work done in Equation (1)

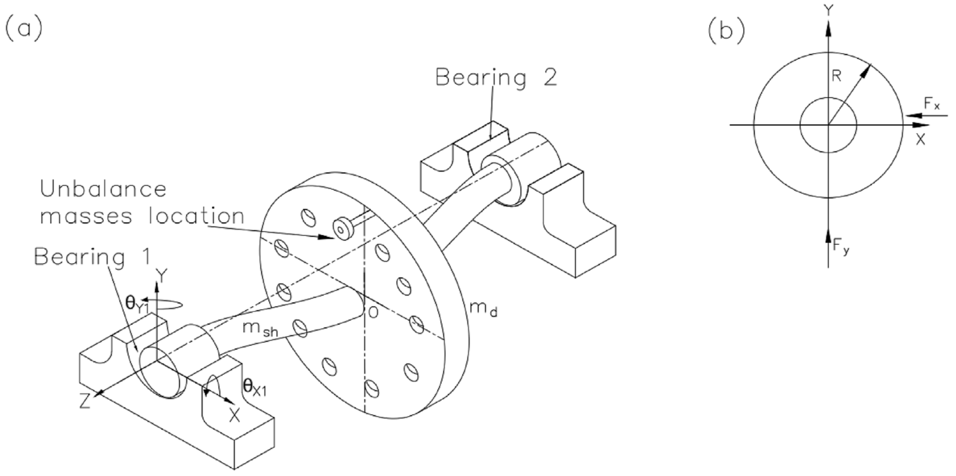

Fig. 1. Elastic rotor-bearing system: (a) schematic of the system and (b) cartesian coordinate of the system.

(Laha, 2010), a small element of volume for the continuous system is considered. Lagrangian coordinates are employed. Finally, the equation of motion for the system is formulated in terms of displacement, as shown in Equation (2) (Baddour, 2008).

$$[M]\ddot{X} + ([G]\,\Omega + [C])\dot{X} + [K]X = F \qquad (2)$$

where [K], [G], [C], and [M] are the stiffness, gyroscopic, damping, and total mass matrices of the shaft, respectively, see Appendix B. The stiffness and damping coefficients of the bearings are illustrated as a function of rotational speed in Fig. D.1, see Appendix D. X represents the displacement vector. The total mass, gyroscopic mass, damping, and stiffness matrices are assembled for each element of the rotating shaft using 8 × 8 matrices. F is the force vector, constituted by hydrodynamic bearing forces (F_x, F_y), and the rotor's gravitational load at the first and end nodes of the elements of the shaft. The system response can be determined by solving the system equations of motion using MATLAB and the direct integration method (ODE15S). The bearing force derivations are illustrated in Appendix A. Fig. 3 depicts the flowchart detailing the procedures for both static and dynamic calculations in theoretical models.

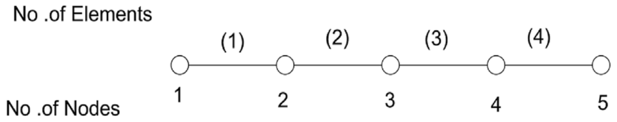

Fig. 2. Number of elements and nodes for the rotating shaft.

Figure 4 shows the corresponding mode shapes for the first four lateral natural frequencies for the studied rotor-bearing system. Fig. 5 presents a Campbell diagram designed to show the system's natural frequency with rotor rotational speeds. The Campbell diagram can be drawn from theoretical/numerical analyses as well as through the actual measurement from the test rig. Critical speeds of the rotor system are determined by estimating eigenvalues for the free vibration case with the rotor-bearing system. The first critical speed of the rotor system is identified as 5047 rpm with a natural frequency of 84.12 Hz. The second critical speed occurs at ~32 455 rpm with a frequency of 540.91 Hz. In addition, it displays the safe operating range for machines.

2. Experimental setup and test rig description

Figures 6 and 7 present authentic photographs of the experimental test rig used in the study, while a schematic diagram of the experimental setup is illustrated in Fig. 8. The shaft, whose geometrical and physical parameters are detailed in Table 1, is prominently featured. The steel shaft is supported by two fluid film hydrodynamic journal bearings, exhibiting a slenderness ratio of 2.5. The physical dimensions and parameters of journal bearings are listed in Table 2. In Fig. 7, it can be observed that pressurized fluid is supplied to the hydrodynamic journal bearing through a static pump. Moreover, the rotor disk is precisely positioned at the shaft mid-span. A three-phase AC electric motor, driven by a variable frequency inverter, is used to change the rotation of the shaft

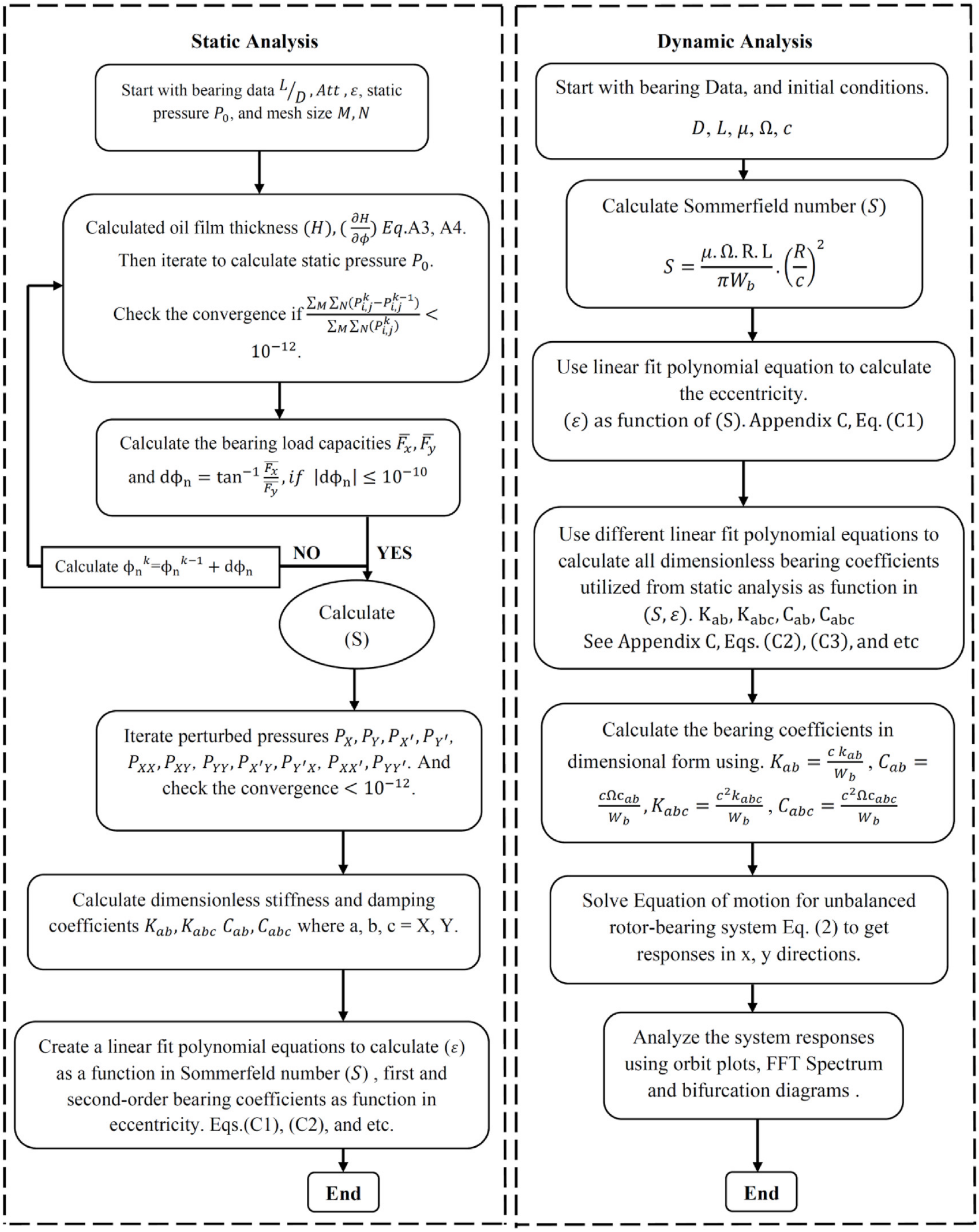

Fig. 3. A flowchart illustrates the analysis used to derive theoretical results.

at varying speed ranges, ranging from 10 to 6000 rpm. For obtaining the shaft x and y, two eddy current probes of the FK-452F model are used. These probes, with a diameter of 16 mm, are securely mounted on a steel frame in a perpendicular configuration. When eddy current probes are brought close to a conductive target, the magnetic field induces eddy current in the target material. These eddy currents, in turn, generate a magnetic field that opposes the original magnetic

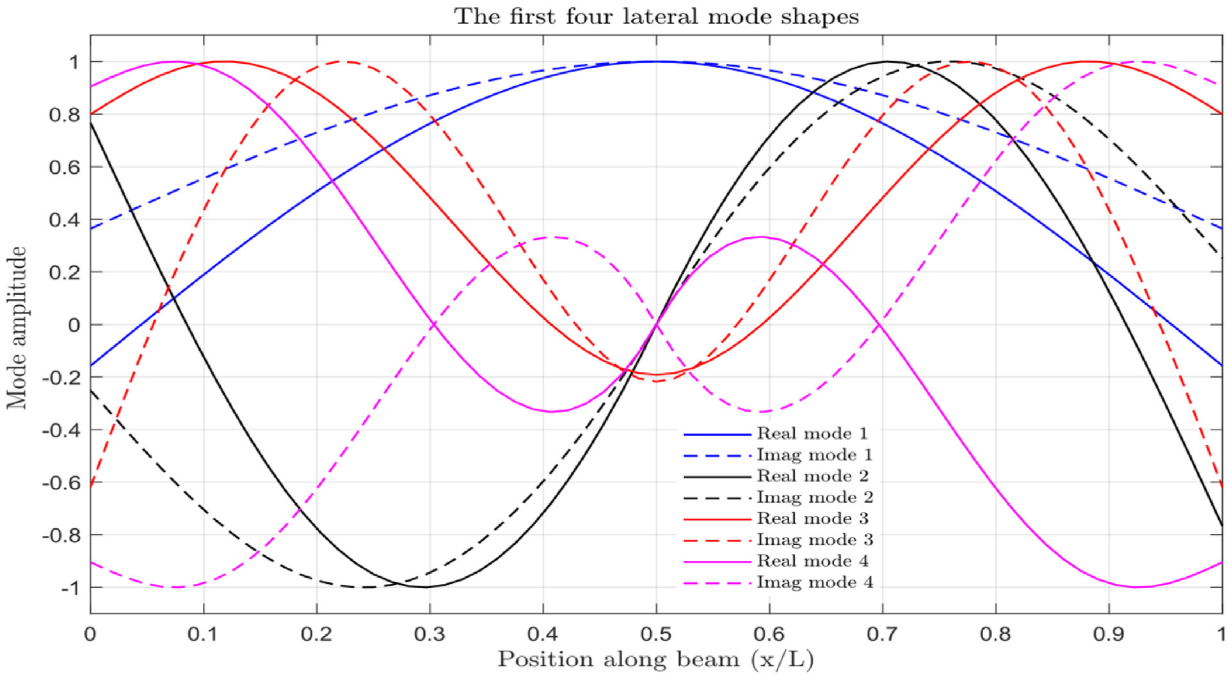

Fig. 4. The corresponding mode shapes for the first four lateral natural frequencies of the studied rotor-bearing system.

field from the coil. This opposition alters the impedance of the coil, which can be measured and converted into a displacement measurement. The signals from the probes are collected and converted using an NI card USB 6216. The data was collected at a sampling rate of 12 800, resulting in a total of 50 031 sampling points. Specifically, the vibration data from the shaft was extracted, with a focus on the initial 10 s of operation. This time frame was chosen to ensure the dataset's integrity and reliability. The system vibration responses are measured by four accelerometers with different sensitivities. Two accelerometers are the ICP-352A60 model, with a sensitivity of 1.02 mV/m/s^2, and the other two are the industrial ICP-603C01 model, with a sensitivity of 10.2 mV/m/s^2. The accelerometers are connected to an NI 9231 sound and vibration module, which is mounted on a Compact-Rio system. The Compact-Rio system transfers the collected and digitized signal to the computer, where the LabVIEW software processes it. For a detailed explanation of the parameters of the instruments and equipment, see Table 3.

3. Theoretical and experimental results

This section presents the results of theoretical and experimental analyses of the rotor-bearing orbit plots and responses. The theoretical analysis uses the bearing forces calculated from the linear and nonlinear coefficients, as well as the nonlinear-bearing forces obtained directly from solving the Reynolds equation. The experimental analysis uses the data collected by LabVIEW from the test rig. Moreover, the section demonstrates the startup and shutdown procedures for the test rig to determine the natural frequencies of the system. Lastly, it briefly examines the bifurcation and waterfall diagrams at bearing and disk locations, and the impact of vibration on the rotor-bearing system at different speeds.

3.1. Rotor orbit plots and response analyses

In this section, we investigate the theoretical results based on the finite-element model and the experimental results from the buildup test rig, including orbit plots and responses of the rotor-bearing system. The dynamic characteristics of the hydrodynamic journal bearing and rotor disk for all studied cases are presented in Table 1, and the fluid properties are detailed in Table 2. Here, $L/D = 2.5$, and Y_d, X_d represent the vertical and horizontal displacements at the disk position, respectively. The first-order analysis predicts a critical speed of 4150 rpm for the system. Below this

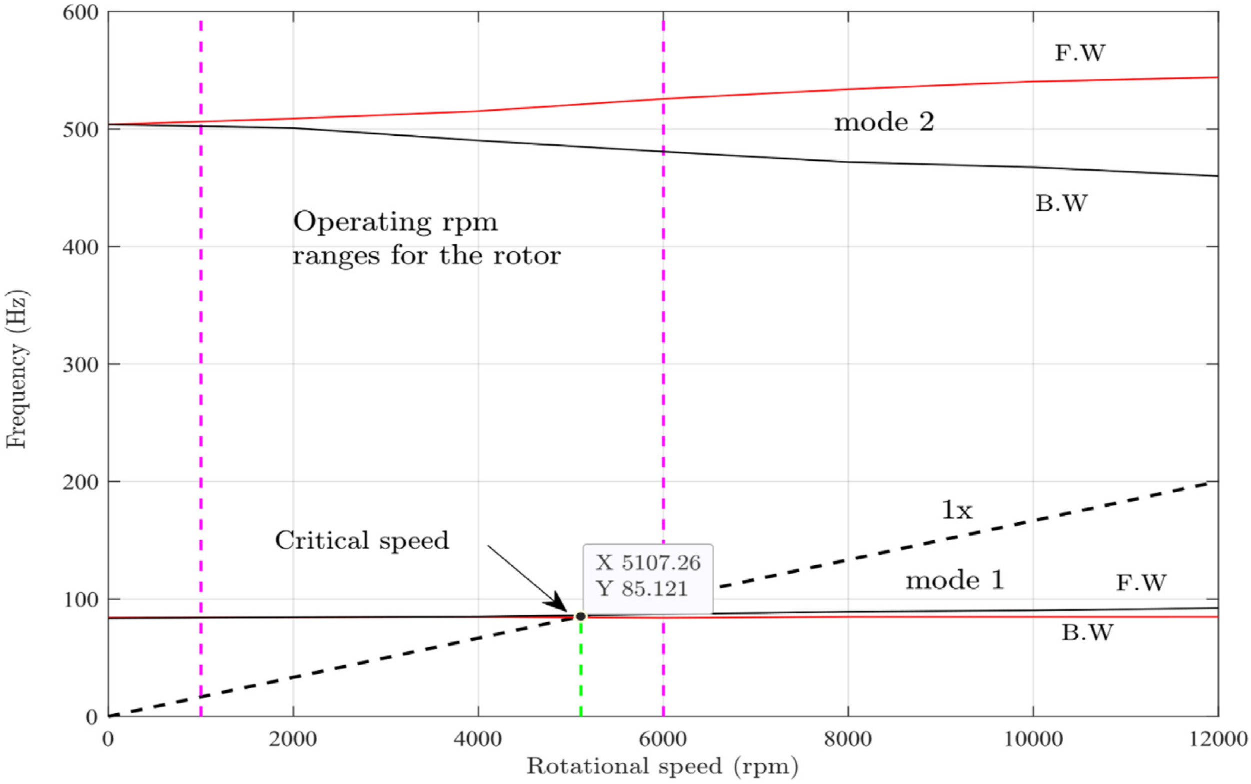

Fig. 5. The Campbell diagram of the studied rotor-bearing system.

speed, the system behaves steadily, but above this speed, it becomes unstable and diverges. The theoretical results are visually represented using color-coded plots. The first-order analysis results, denoted by the color blue, are typically displayed in the first column of Figs. 9, 11, 13, and 15 and are detailed in Table 4. The second-order analysis results, represented in black, are plotted in the second column. Nonlinear analysis results are depicted in red and can be found in the third column of the figures. The bearing stiffness and damping coefficients were determined for both first-order and second-order studies, as described in Ahmed et al. (2023), and briefed in Ahmed et al. (2023). The solution based on nonlinear-bearing forces is presented in the third column, and these bearing forces are calculated by solving the Reynolds equation at each time step. For experimental results, real measurements are displayed in the first column (a) of Figs. 10, 12, 14, and 16. The second column (b) illustrates the real measurements after applying a low-pass smooth filter to eliminate noise. The third column (c) presents the responses of the studied cases over time (time-domain) plots. Finally, the last column (d) shows the frequencies of each case at the operating speed. Figs. 9 and 10 panels (a), (b), and (c) show theoretical and experimental orbit plots and responses for the rotor-bearing system at different speeds with a system unbalanced mass of 7.02×10^{-4} kg. Fig. 9 shows that all analyses provide the same steady-state orbits and responses as indicated in the panels of the first three columns. At speeds less than the critical speed, a stable orbit was created with different orbit radii of 0.041, 0.14, and 0.18 mm, respectively. The vibration response represents steady-state amplitude over time. As the rotational speed increases gradually, the second-order analyses differ in the orbit shape as shown in Fig. 9 panels (f) and (j). For Fig. 10, the top row depicts the orbits and responses at an operational speed of 1000 rpm, the middle row at 2000 rpm, and the bottom row at 3000 rpm. All panels show a stable rotor orbit in steady-state conditions with a limit cycle radius of $\sim$0.1 mm. Fig. 11 panels a, b, c, and d illustrate the rotational speed of 4000 rpm and unbalanced mass of 7.02×10^{-4} kg·m. The first-

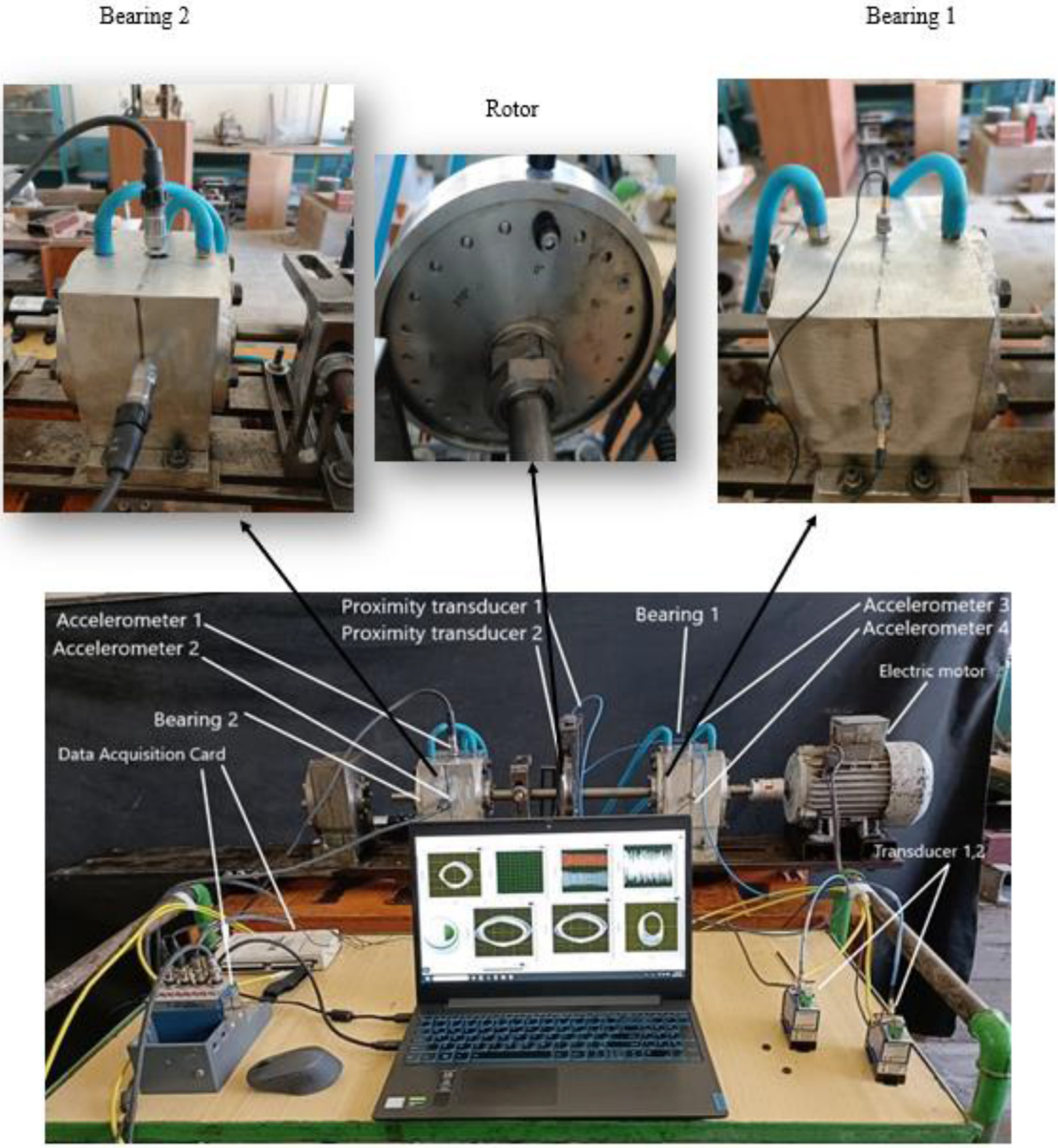

Fig. 6. A photograph depicting the experimental test-rig utilized for testing the rotor, supported by two journal bearings.

order, second-order, and nonlinear analyses show trajectories different in amplitude and shape as depicted. Fig. 12 panels a, b, and c display the experimental findings. The oil whip phenomenon occurs when the whirling rotor passes through or close to one of the critical speeds. This oil whip is a destructive journal-bearing phenomenon. When the speed increases to 5000 rpm as plotted in Fig. 11, panels e and f, it shows an increase in the orbit radius and the amplitude of vibration in the analyses based on the first-order and second-order effects. It indicates that the system is unstable and

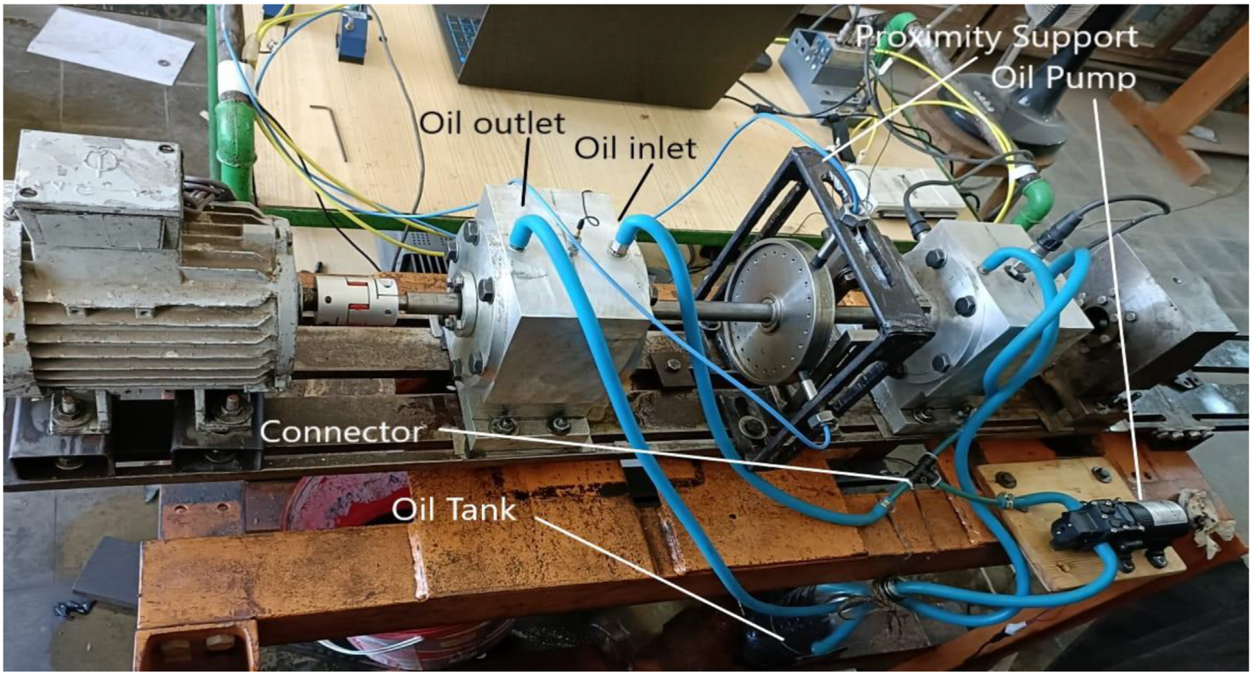

Fig. 7. A rear view photograph providing additional details and insights into the machine.

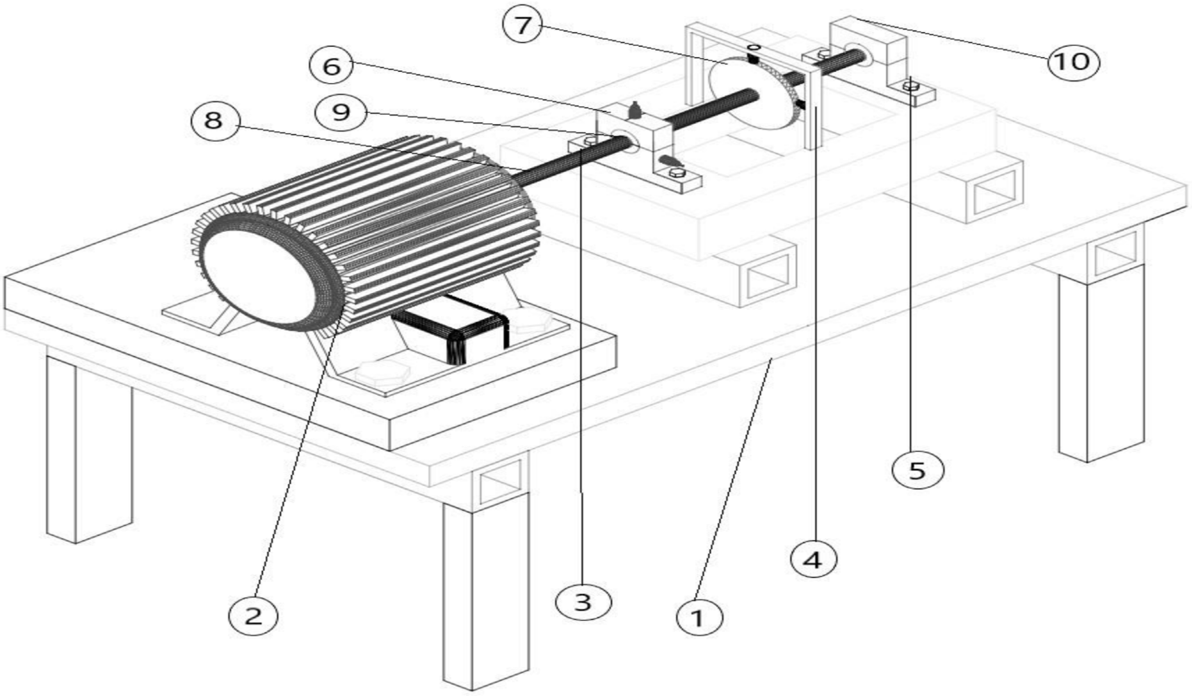

(1) Steel Base.
(2) 1 kW AC motor
(3) Rotating shaft.
(4) Proximity support.
(5) Journal bearing.
(6) Accelerometer.
(7) Rotor disk
(8) Rigid coupling.
(9) Bearing sleeve.
(10) Journal bearing housing.

Fig. 8. Schematic diagram illustrating the test rig setup.

Table 1. Rotor-bearing dynamic characteristics for simulation.

Parameters	Value
Shaft diameter	20 mm
Rotating shaft length	0.5 m
Modulus of elasticity	2.0e+11 Pa
Density	7850 kg/m^3
Bearing radial clearance	250 μm
Bearing mass	3.35 kg
Disk mass	1.5 kg
Viscosity of lubricant	0.031 Pa·s
Slenderness ratio	2.5

Table 2. Parameters for the fluid film used in this work.

Parameters	Value
Oil viscosity (Pa·s)	0.031
Supply oil temperature (°C)	25
Supply oil pressure (Mpa)	0.1
Oil type	ISO-VG32

begins to diverge, but in the nonlinear analysis, the system displays acceptable agreement with the experimental orbit in the second row of Fig. 12. The amplitude and radius of the orbit for first-order and second-order analyses decrease as depicted in Fig. 11, panels (i to l), and the nonlinear analysis displays good agreement in the amplitude and the orbit shape with the experimental work presented in the third row of Fig. 12. At a rotational speed of 6000 rpm, the third row of Fig. 12 shows that the analyses based on the first-order and the second-order have amplitudes and orbit radii smaller than the case of 5000 rpm. This behavior has several reasons: the first one is that the rotor has natural frequencies that coincide with the operating speed range. When the system operates near these resonant frequencies, the response can be significantly amplified. As the speed increases beyond the resonant region, the response decreases. The second reason is that the rotor-bearing system stiffness and damping can also affect the response. At lower speeds, the system may exhibit lower stiffness and damping, resulting in higher responses. However, as the speed increases, the stiffness and damping effects become more dominant, leading to a decrease in the response (Rao and Yap, 1995). To study these cases and determine the system's natural frequencies, the equations were numerically solved. The first natural frequency was recorded as 85.12 Hz, as shown in Table 5. Moreover, start-up and shut-down processes were investigated to obtain the natural frequencies of the system experimentally, as displayed in Fig. 17. The first natural frequency is observed to resonante with a rotational speed of 5845 rpm. Fig. 12 illustrates the FFT plot showing the subsynchronous peaks at low frequency as a result of the mechanical looseness of rotor-bearing system parts, and super-synchronous at a frequency equal to 2X. This is pointed to an excitation frequency close to the first critical frequency. Fig. 18 shows a comparative study between theoretical and experimental frequency spectra for two rotational speeds and the results show good agreement.

Figures 13 and 14 display the theoretical and experimental trajectories and responses at rotational speeds below the critical speed, with an increased unbalanced mass totaling 8.6 × 10^{-4} kg·m. The unbalanced mass was augmented by adding small masses to threaded holes with a diameter of 5 mm located on the rotor. The augmentation aimed to study the effect of the added unbalanced masses on the rotor-bearing system behavior. In Fig. 13 gives the radius of the orbit and amplitude measure 0.13

Table 3. Parameters of instruments and equipment.

Parameters	Ranges	Sensitivity	Model
AC motor	1 Hp, 2850 rpm	–	AOI
Proximity transducers	0.5 mm: 5 mm from sensor tip	3.94 V/mm	Eddy current probes FK-452F
Accelerometers	±4905 m/s^2, 5: 60 000 Hz	1.02 mV/m/s^2	ICP-352A60
	±490 m/s^2, 0.5 : 10,000 Hz	10.2 mV/m/s^2	Industrial ICP-603C01
NI card	1 : 10 mV, 16 analog ports	–	NI card USB 62164
Compact RIO	Sample rate 51.2 kS/s frequency 13.1072 MHz, 8 analog channels	3.7 ppm/°C, 22.4 ppm/°C	NI 9231 sound and vibration module
Power supply	0 : 30 V, 1.5 A	–	B & J Dual DC (P 301 5D)
Inverter	220 V: 240 V ± 10%, 1 ph/3 ph, 50 : 60 Hz ± 5%	–	MOVITRAC LT E
		–	
Oil pump	0.1–1 bar,4.0 LPM, 15 V	–	Aqua head (HF-8367)

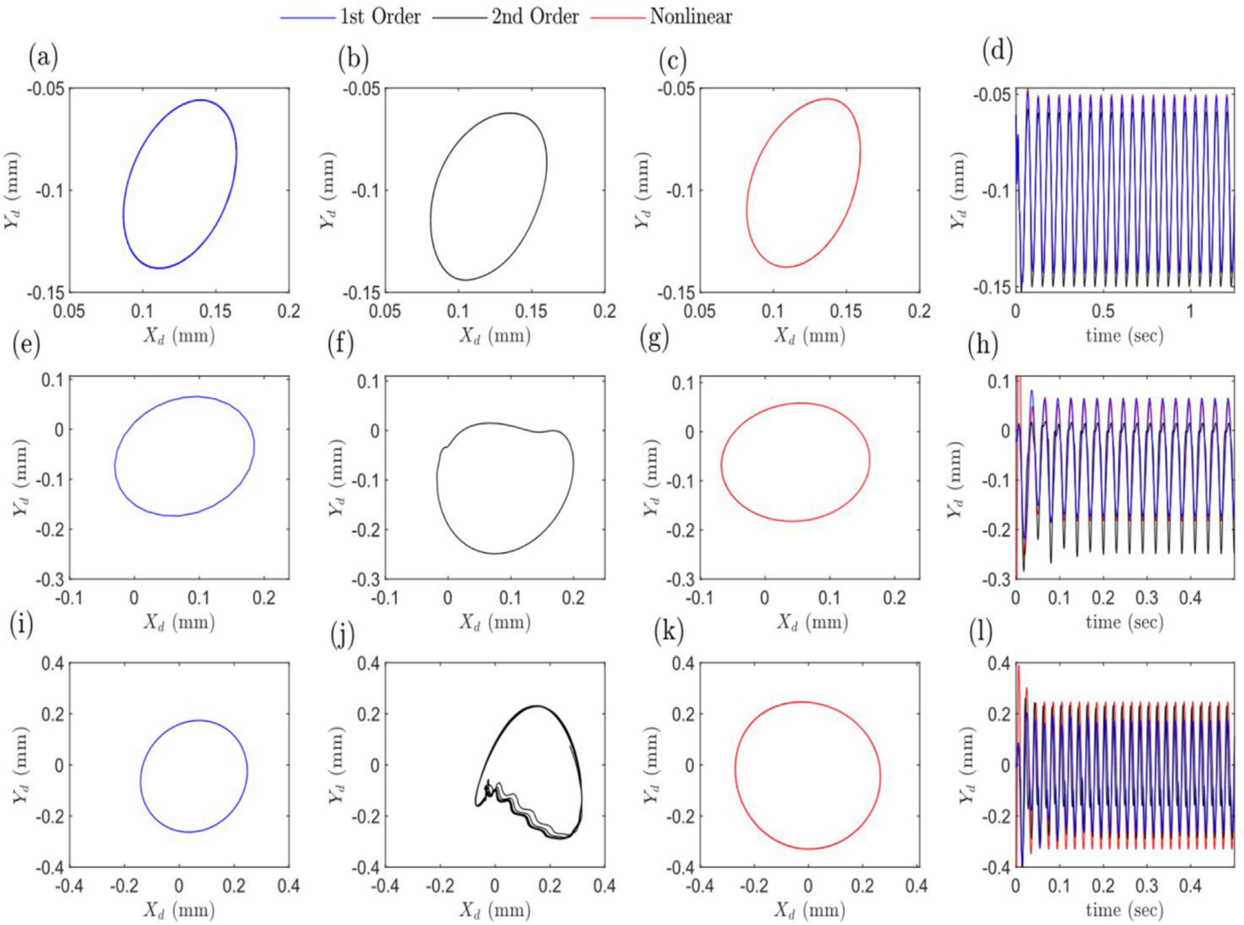

Fig. 9. Theoretical results for orbit plots and responses of vertical displacement at the disk position with an unbalanced mass of 7.02 × 10^{-4} kg·m. Panels (a–d) represent cases at a shaft speed of 1000 rpm; panels (e–h) represent cases at a shaft speed of 2000 rpm, and panels (i–l) represent cases at a shaft speed of 3000 rpm.

and 0.15 mm at 1000 and 2000 rpm, respectively. However, at 3000 rpm, the orbit radius increases to 0.37 mm. Fig. 14 illustrates that all panels in the top, middle, and bottom rows exhibit the same steady-state response, with an orbit radius of ~0.15 mm, consistent with the discussion in Fig. 9.

Figures 15 and 16 provide detailed insights near and above the critical speed. Fig. 15 shows that the orbit radius increases to 0.41 mm in the first-order analysis, 0.56 mm in the second-order analysis, and 0.84 mm in the nonlinear analysis when the shaft rotational speed reaches 4000 rpm. As the system's rotational speed continues to increase, it eventually surpasses the first theoretical resonant speed of 5107 rpm as listed in Table 4. Consequently, the system's vibration amplitude significantly increases, followed by a decrease after exceeding the resonant speed, as depicted in the third row of Fig. 15. Fig. 16 illustrates the speed increasing from 4000 to 6000 rpm, with the system's orbit plots gradually expanding from a radius of 0.3 mm until reaching the limit cycle with a radius of 0.5 mm at a speed of 6000 rpm. The experimental results exhibit acceptable agreements with the theoretical results in the orbit shapes across all cases but vary in amplitudes. Upon comprehensive analysis, it becomes evident that the nonlinear analysis aligns most closely with the experimental results in terms of orbit limit circle and amplitudes.

3.2. Monitoring of the experimental test rig startup and shutdown process

This section introduces the vibration monitoring during startup and shutdown of the test rig used to measure the experimental natural frequencies of

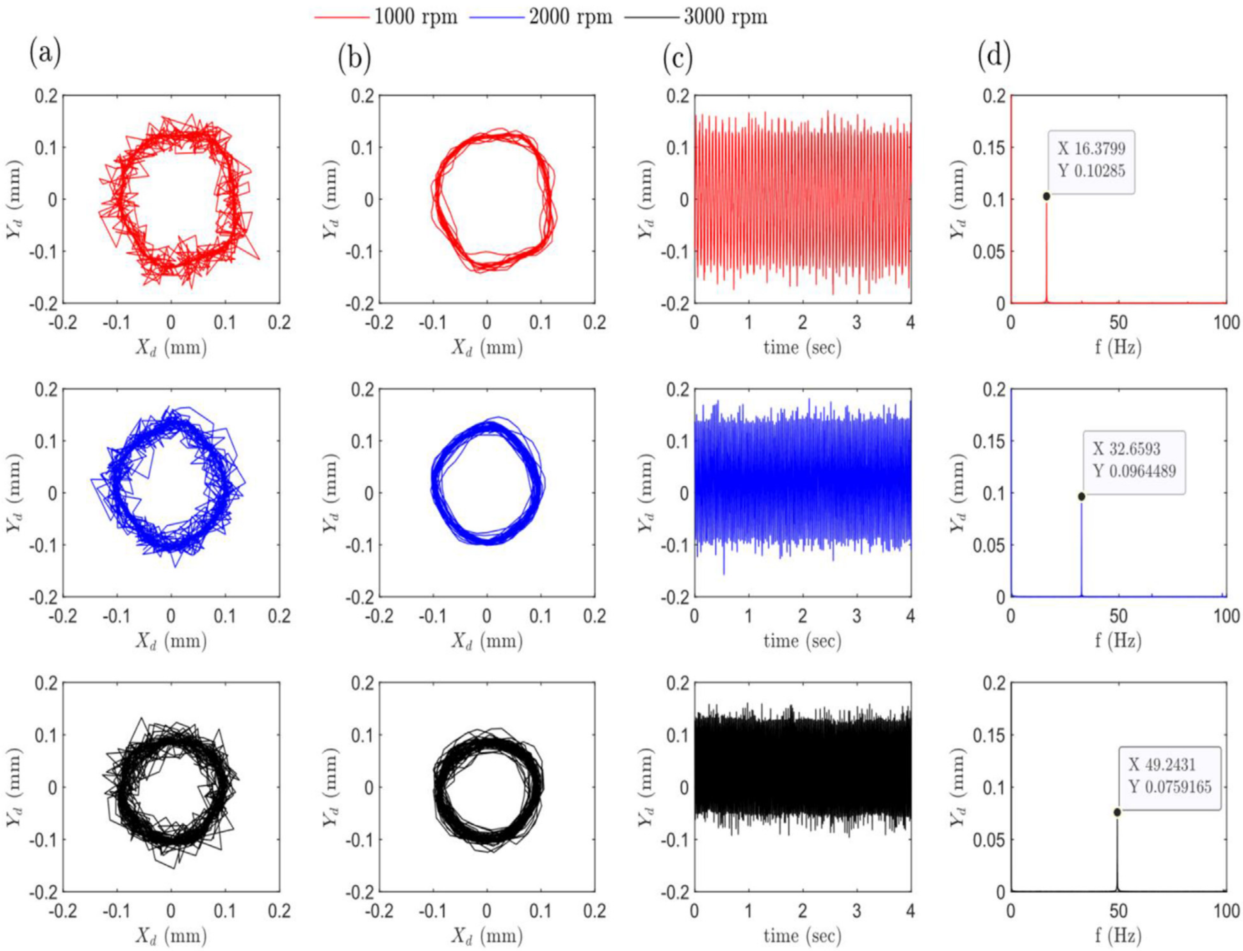

Fig. 10. *Experimental results for orbit plots and responses of vertical displacement at the disk position with an unbalanced mass of* 7.02×10^{-4} *kg·m at various shaft speeds; panel (a) shows the real orbit plots; panel (b) displays orbits with a smoothing filter; panel (c) exhibits time responses of vertical displacement, and panel (d) presents FFT spectra. FFT, fast fourier transform.*

the studied rotor-bearing system, as illustrated in Fig. 17 panels (a) and (c), respectively. Startup and shutdown processes refer to the sequences of actions or procedures that occur when a rotor-bearing system is powered down (shut down) and then powered up (started up). These processes are crucial for accurately determining the peak amplitudes of the system (Hamdoon et al., 2012). The highest amplitude corresponds to the first natural frequency of the system, as depicted in the plots of Fig. 17b and d. In Fig. 17b, the startup process reveals a first natural frequency of 97.45 Hz, corresponding to 5847 rpm, while in Fig. 17d, the shutdown process shows a first natural frequency of 97.41 Hz, corresponding to 5844 rpm. Fig. 4 displays the theoretical first four mode shapes and the corresponding natural frequency of the system. The first natural frequency is 85.12 Hz (5107 rpm) as listed in Table 5. By comparing the experimental and theoretical first natural frequencies, it can be concluded that the system's resonant speed occurs when the speed is gradually increased from 5000 to 6000 rpm.

3.3. Bifurcation and waterfall diagrams for studied cases

This section explores bifurcation analysis and three-dimensional spectra for an unbalanced rotor supported by two identical journal bearings, based on second-order and nonlinear analyses. The study was conducted at two locations: one at the disk

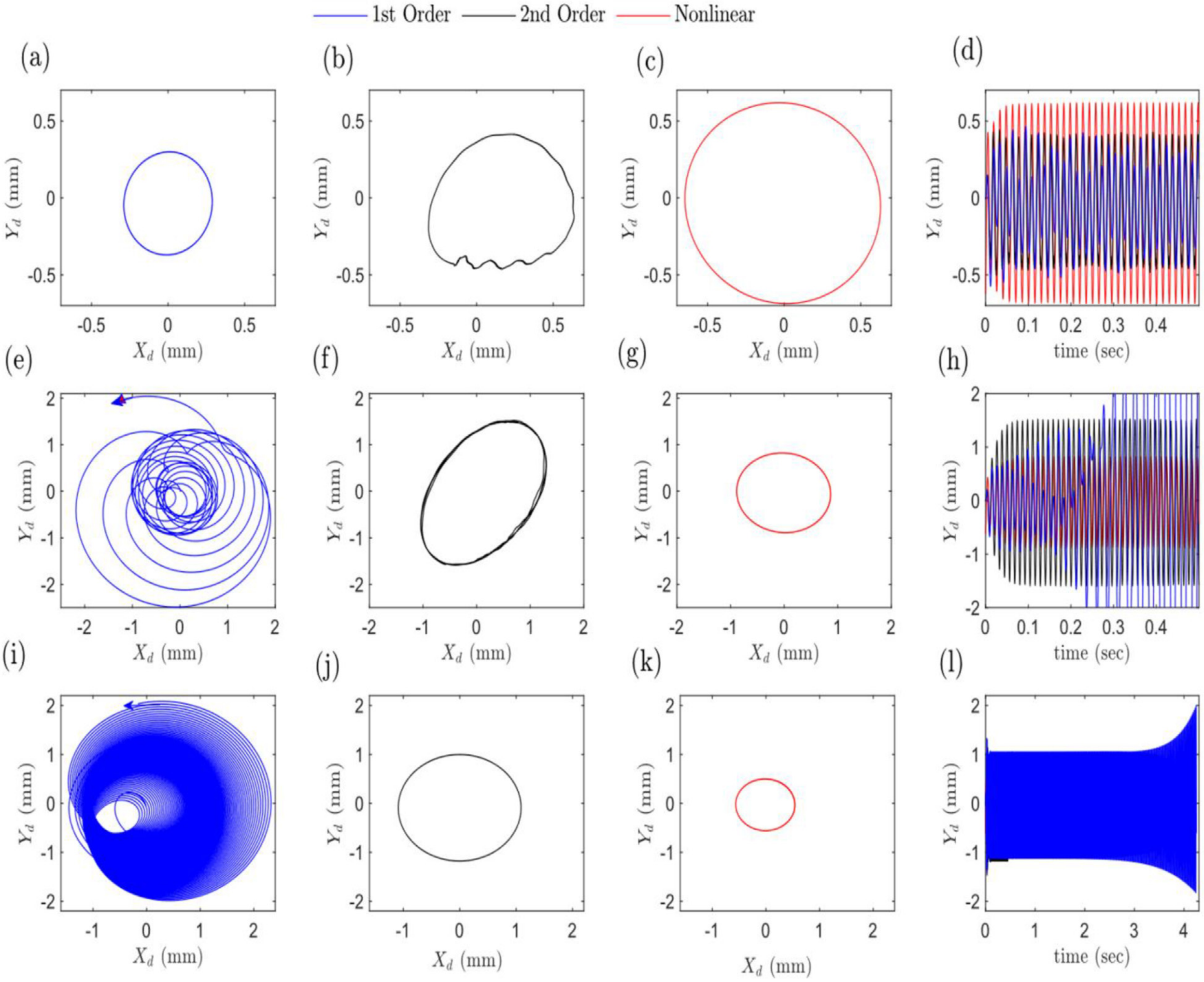

Fig. 11. Theoretical results for orbit plots and responses of vertical displacement at the disk position with an unbalanced mass of 7.02 × 10^{-4} kg·m. Panels (a–d) represent cases at a shaft speed of 4000 rpm; panels (e–h) represent cases at a shaft speed of 5000 rpm; and panels (i–l) represent cases at a shaft speed of 6000 rpm.

location and the other at the bearing location, as depicted in Figs. 19–22. These figures illustrate areas of high amplitude corresponding to increasing shaft rotational speeds. The shaft speed was gradually increased with a constant step of 200 rpm. The rotor-bearing system under investigation was exposed to unbalanced forces, a common occurrence in real-world applications, which induced dynamic instability and affected its performance. The product of the unbalanced masses and the eccentric distance are $m \times e = 7.02 \times 10^{-4}\text{kg}\cdot\text{m}$ and $8.6 \times 10^{-4}\text{kg}\cdot\text{m}$, respectively.

Figure 19 panels (a) and (b) display bifurcation and waterfall plots for the first case based on a second-order analysis at the disk location. These plots depict amplitude changes over a speed range from 1000 to 6000 rpm, with significant changes around 5350 rpm, indicated by the vertical red line. When the unbalanced mass was increased to $8.6 \times 10^{-4}\text{kg}\cdot\text{m}$, the system behavior did not show a significant change, as evident in panels (c) and (d) of the second row of Fig. 19. Fig. 20 panels (a), (b), (c), and (d) demonstrates bifurcation and waterfall diagrams at the bearing location. Analytically, when

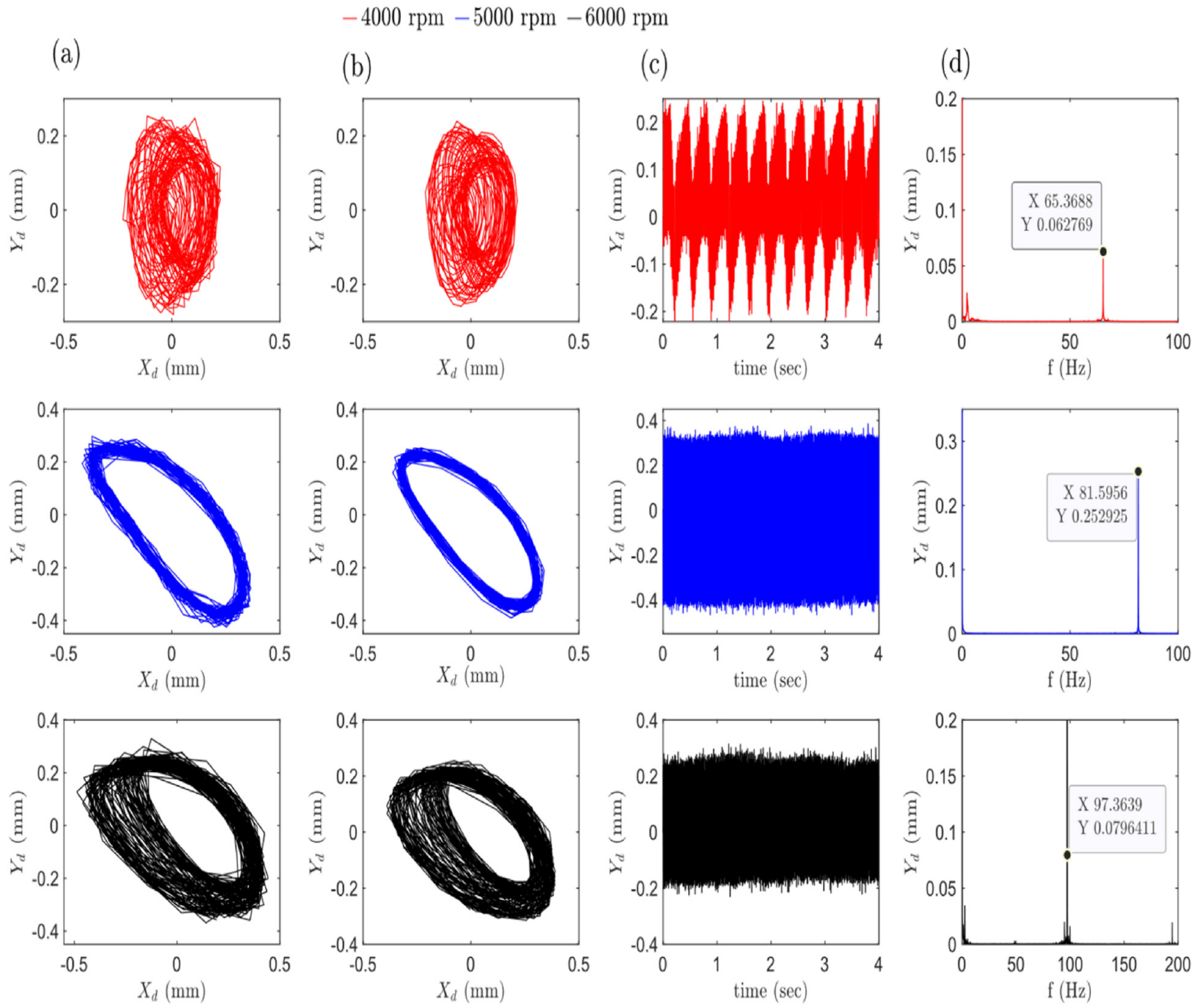

Fig. 12. Experimental results for orbit plots and responses of vertical displacement at the disk position for various shaft speeds with an unbalanced mass of 7.02 × 10^{-4} kg·m. Column (a) shows the real orbit plot; column (b) displays the orbit with a smooth filter; column (c) presents time responses of vertical displacement; and column (d) exhibits the FFT spectrum. FFT, fast fourier transform.

the shaft rotates at one of its resonance speeds, the steady-state limit cycle of the bearings exceeds the clearance circle. The horizontal red lines in the figure indicate the boundaries of the bearing's clearance circle. While this phenomenon observed in the bifurcation at the bearing location is practically impossible, the bifurcation and waterfall diagrams at both disk and bearing locations for the two unbalanced masses exhibit similar behavior in terms of amplitude and plot shape for second-order analysis. Fig. 21 shows the results of the nonlinear analysis for two unbalanced masses: $7.02 \times 10^{-4}\mathrm{kg \cdot m}$ and $8.6 \times 10^{-4}\mathrm{kg \cdot m}$. Panels (a) and (b) represent $7.02 \times 10^{-4}\mathrm{kg \cdot m}$ case, and panels (c) and (d) represent the $8.6 \times 10^{-4}\mathrm{kg \cdot m}$ case. These panels illustrate bifurcation and waterfall plots depicting the behavior of the rotor-bearing system. The plots show a good agreement with the second-order analysis in terms of shape, with a notable increase in the amplitude attributed to the added unbalanced mass. This increase is primarily due to the unbalanced mass added to the holes on the disk surface at zero angles, as shown in Fig. 6, which amplifies the centrifugal forces acting on the disk. Figs. 19–22 panels b and d: waterfall diagrams for both second-order and nonlinear analyses. Due to

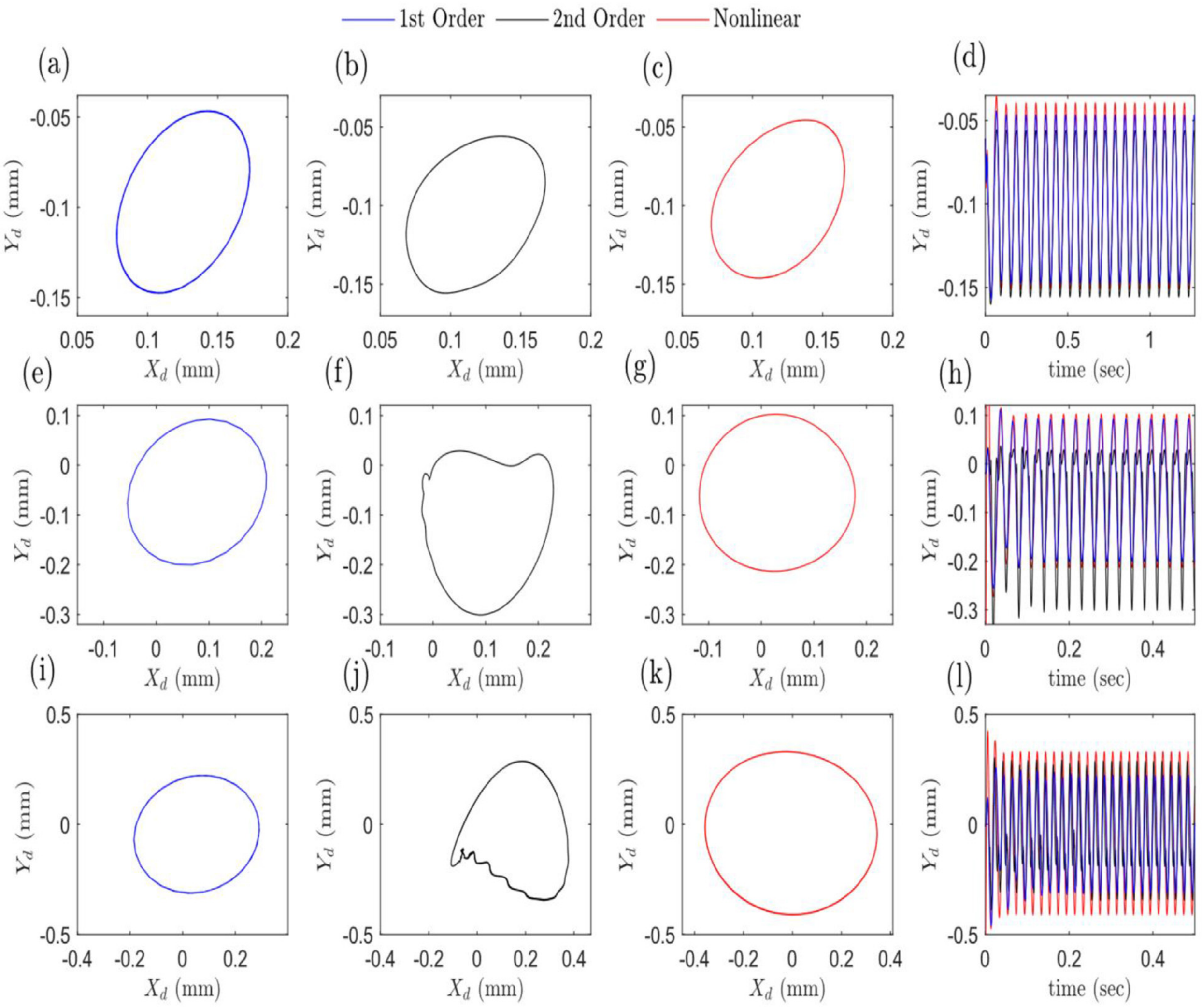

Fig. 13. Theoretical orbit plots and responses of vertical displacement at the disk position with an unbalanced mass of 8.6 × 10^{-4} kgm. Panels (a–d) represent cases at a shaft speed of 1000 rpm; panels (e–h) represent cases at a shaft speed of 2000 rpm; and panels (i–l) represent cases at a shaft speed of 3000 rpm.

the simple design of journal bearings and the disk, three-dimensional frequency domain features of vibration signals are good for overall investigations. For all studied cases, waterfall panels (b and d), the amplitude peaks increase with the speed runup until they reach almost the first critical frequency, subsequently, the frequency spectrum of the healthy operation becomes apparent, and the amplitude of peaks decreases.

3.4. Vibration analyses for unbalanced rotors

Vibration due to rotor unbalance is a common issue in rotating machinery, easily detectable and correctable. Unbalanced rotors typically exhibit a series of harmonics at running speeds in journal bearings. The FFT spectrum of unbalance resembles that of mechanical looseness, as the frequencies of signals at different shaft speeds are akin to those produced by mechanical looseness (Scheffer and Girdhar, 2004). Even minor unbalance or misalignment can lead to higher vibration amplitudes. Fig. 23 shows the responses and FFT spectrum for an unbalanced rotor operating at speeds below the critical speed. The figures are color-coded: red for 1000 rpm and blue for 2000 rpm. Signals from horizontal and vertical sensors at two supporting hydrodynamic journal

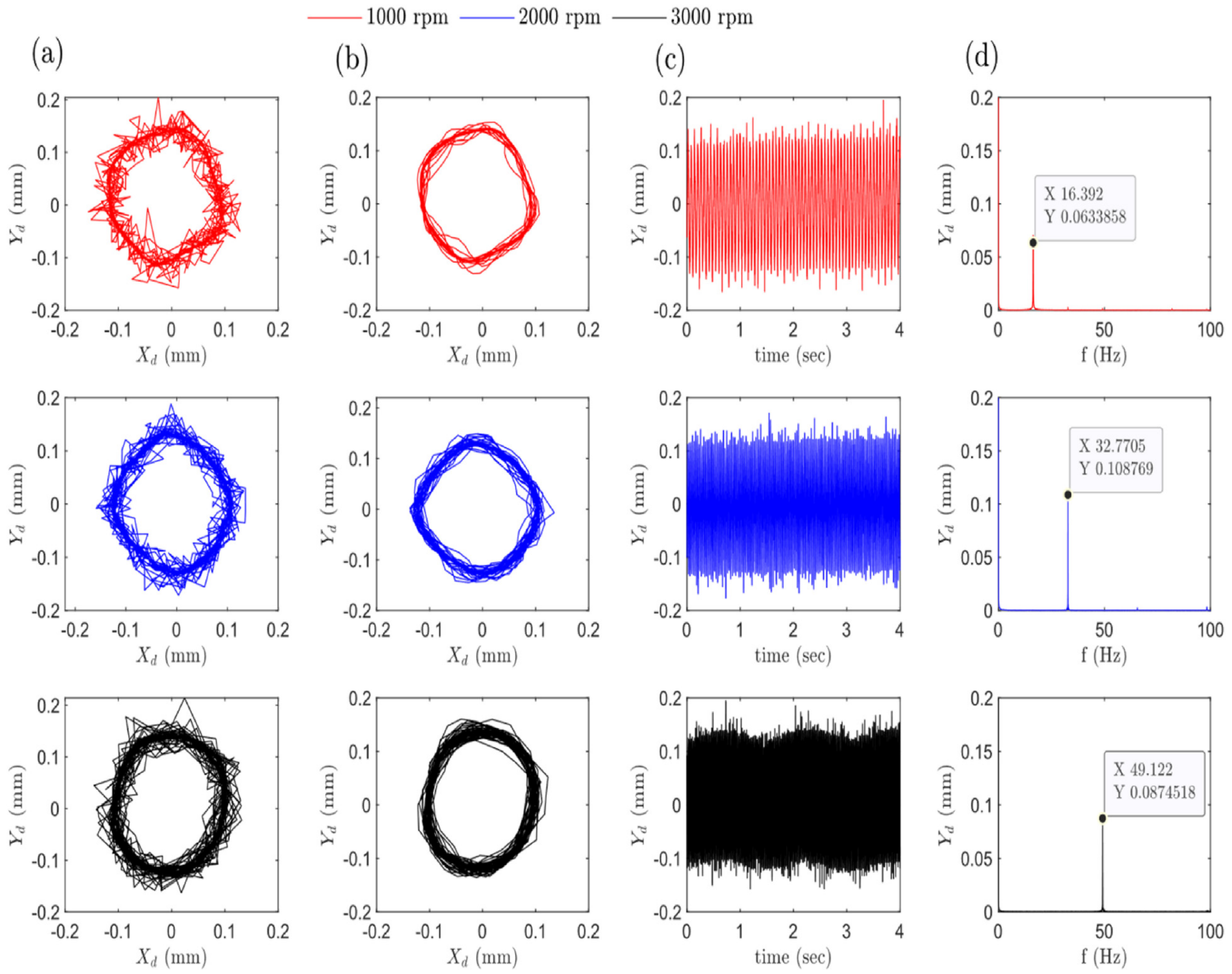

Fig. 14. Experimental orbit plots and responses of vertical displacement at the dis position for different shaft speeds with an unbalanced mass of 8.6×10^{-4} *kg·m. Columns (a) show real orbit plots, (b) display orbits with a smooth filter, (c) depict time responses of vertical displacement, and (d) illustrate the FFT spectra. FFT, fast fourier transform.*

bearings were analyzed. Vertical sensor amplitudes are almost identical, while the horizontal sensor near the motor exhibits a slightly lower amplitude, attributed to minor misalignment and unbalance, visually evident in panels (a, b, c, and d) and also (i, j, k, and l). The FFT spectrum in Figures (e, f, g, and h) and (m, n, o, and p) reveals signs of mechanical looseness and minor rotor rub. As the rotational speeds increase to 3000 rpm in Fig. 24 panels (a, b, c, and d), vibration amplitudes remain consistent. In panels (e, f, g, and h) approaching the critical speed introduces notable structural and mechanical looseness, with the highest amplitude reaching 3X. Panels (i, j, k, and l) and (m, n, o, and p) demonstrate speeds close to the critical limit, where synchronous rotor response (1X displacement at) peaks. Fig. 25a–d and (i, j, k, and l) for the time domain, and (e, f, g, and h) and (m, n, o, and p) for the FFT spectrum illustrate rotor run-up above the critical speed, where synchronous and undesired vibration affects the system Mechanical looseness and misalignments are evident. The results emphasize the importance of addressing rotor-bearing systems near their first balance resonance. Operating at these speeds exacerbates issues with unbalance

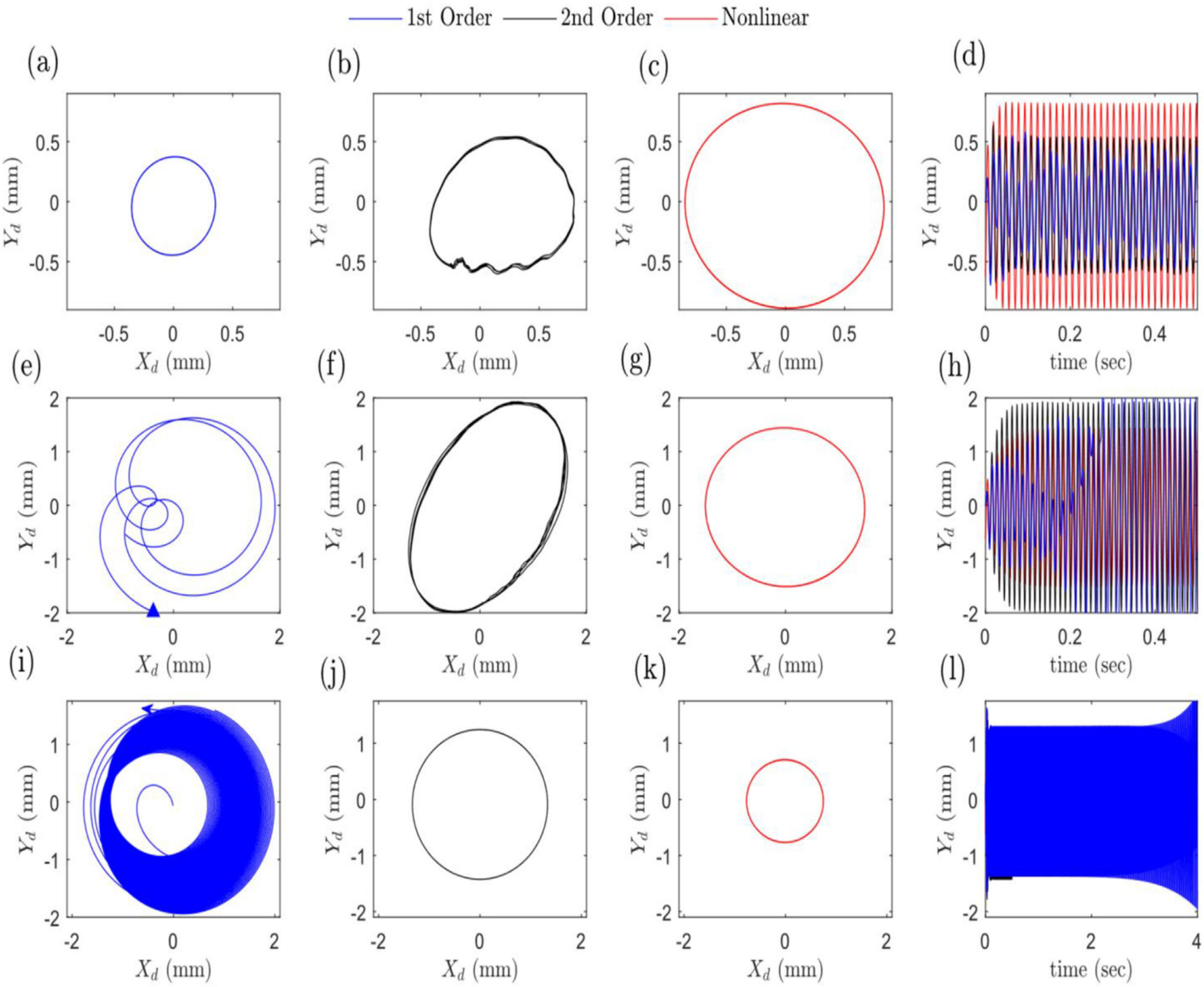

Fig. 15. Theoretical orbit plots and responses of vertical displacement at the disk position with an unbalanced mass of 8.6 × 10^{-4} kg·m. For all cases, (a, b, c, and d) represent cases at a shaft speed of 4000 rpm (e, f, g, and h) represent cases at a shaft speed of 5000 rpm, and (i, j, k, and l) represent cases at a shaft speed of 6000 rpm.

Table 4. Studied cases for system trajectories and responses for unbalanced mass for the system equals 7.02 × 10^{-4} kg·m and another unbalanced mass equals 8.6 × 10^{-4} kg·m, respectively.

Operating cases	Operating speed (rpm)	Sommerfeld number (S)	Eccentricity ratio ε
Figs 6, 10a, b, c, d	1000	0.0617	0.557
Figs 6, 10e, f, g, h	2000	0.1235	0.317
Figs 6, 10i, j, k, l	3000	0.1852	0.215
Figs 7, 11a, b, c, d	4000	0.2469	0.170
Figs 7, 11e, f, g, h	5000	0.3086	0.047
Figs 7, 11i, j, k, l	6000	0.3704	0.216

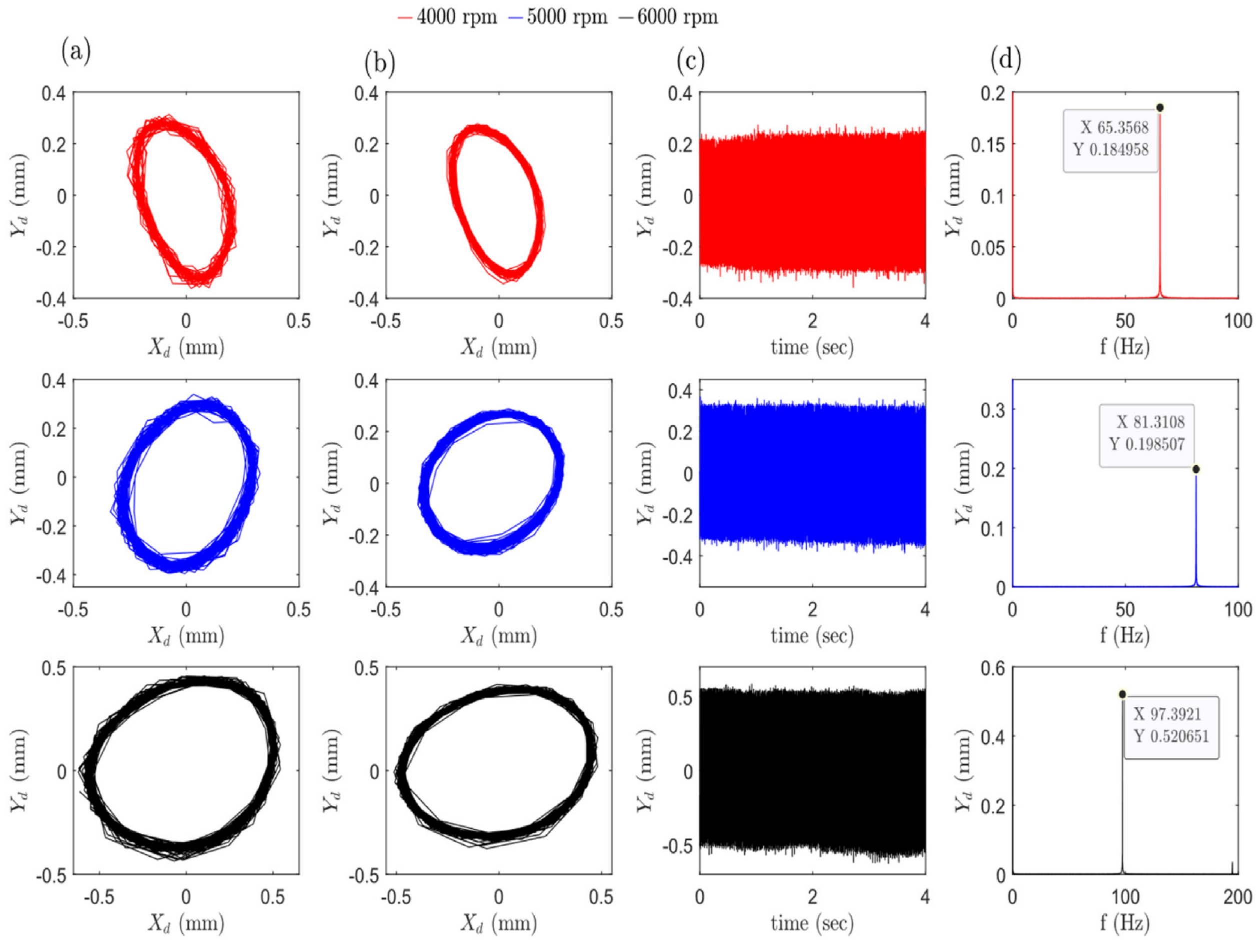

Fig. 16. Experimental orbit plots and responses of vertical displacement at the disk position with an unbalanced mass of 8.6 × 10^{-4} kg·m. For all cases, column (a) shows a real orbit plot, column (b) displays orbits with a smooth filter, column (c) presents time responses of vertical displacement, and column (d) shows the FFT spectra. FFT, fast fourier transform.

Table 5. The first two lateral natural frequencies for the studied rotor-bearing system at several rotational speeds.

Rotational speed (rpm)	First mode N.F. (Hz)	Second mode N.F. (Hz)
1000	−19.390 + 84.028i	−71.287 + 503.21i
2000	−18.690 + 84.056i	−70.920 + 508.26i
3000	−18.690 + 84.056i	−70.920 + 508.26i
4000	−33.248 + 84.480i	−70.920 + 508.26i
5000	−33.248 + 84.480i	−70.920 + 508.26i
6000	−32.389 + 84.986i	−70.920 + 508.26i

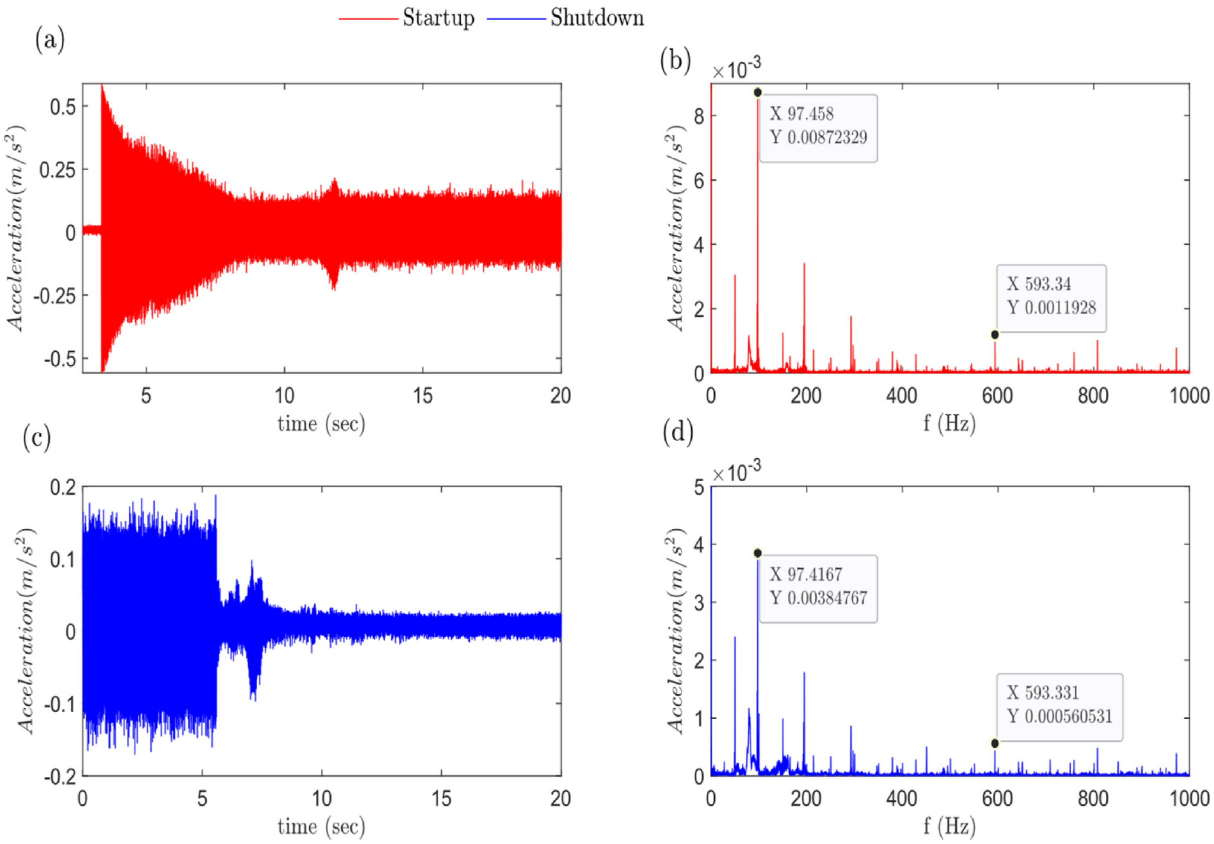

Fig. 17. Startup and shutdown processes of the experimental test rig, panels (a) and (b) show the time domain and FFT spectrum for startup, while panels (c) and (d) display the time domain and FFT spectrum for the shutdown process. FFT, fast fourier transform.

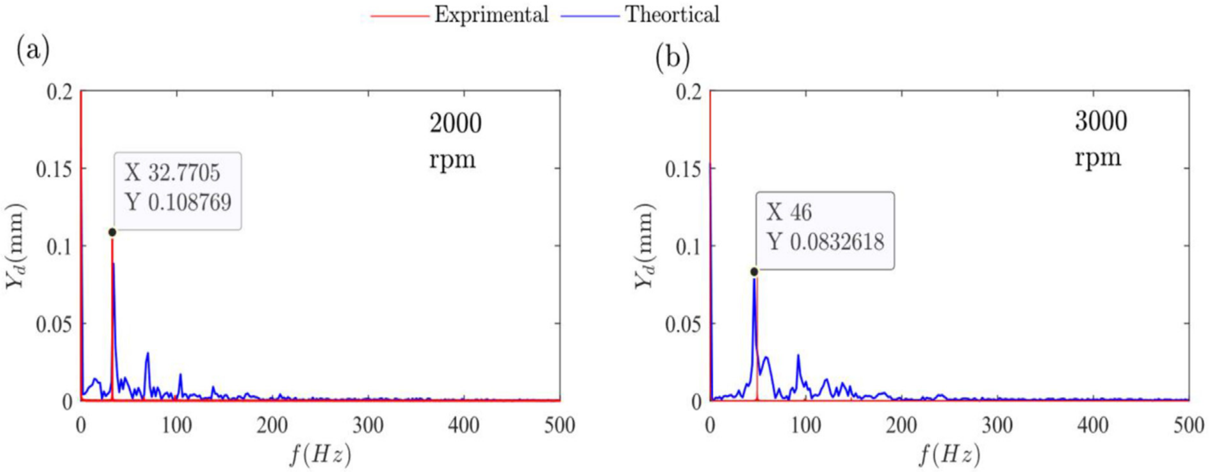

Fig. 18. Comparison between the theoretical and experimental results using FFT of two rotational speeds: panels (a) and (b) FFT spectrum for 2000 and 3000 rpm, respectively. FFT, fast fourier transform.

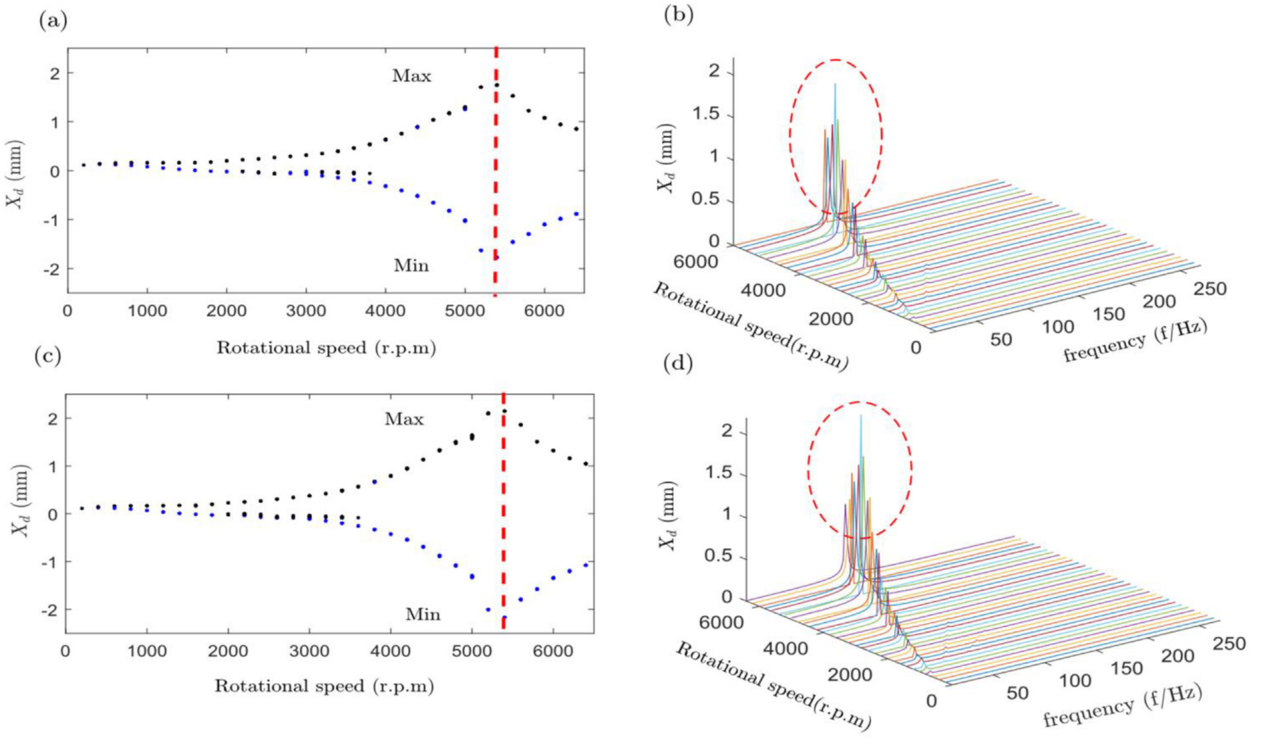

Fig. 19. Bifurcation and waterfall plots for the rotor-bearing system based on second-order analysis at the disk location. Panels (a, c) depict bifurcation diagrams, and panels (b, d) display three-dimensional spectrum diagrams for two unbalanced masses: $7.02\text{x}10^{-4}\ kg\cdot\text{m}$ *and* $8.6\text{x}10^{-4}\ kg\cdot\text{m}$, *respectively.*

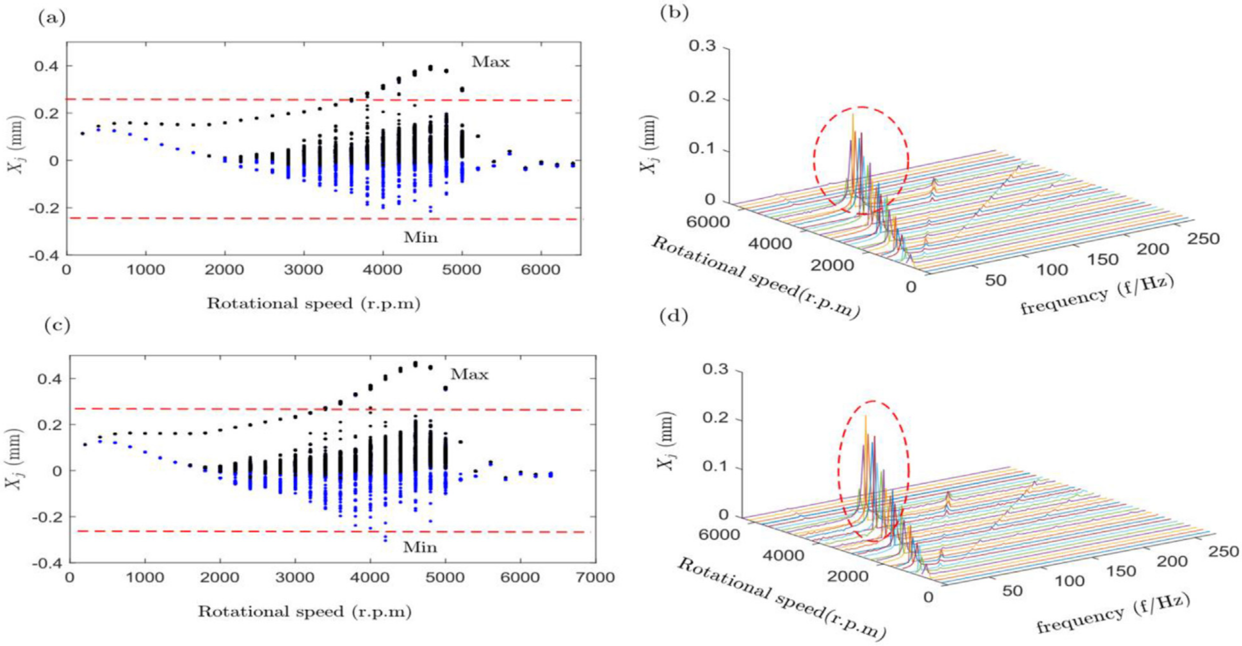

Fig. 20. Bifurcation and waterfall plots for the rotor-bearing system based on second-order analysis at the bearing location. Panels (a, c) depict bifurcation diagrams, and panels (b, d) display three-dimensional spectrum diagrams for two unbalanced masses: $7.02\text{x}10^{-4}\ kg\cdot\text{m}$ *and* $8.6\text{x}10^{-4}\ kg\cdot\text{m}$, *respectively.*

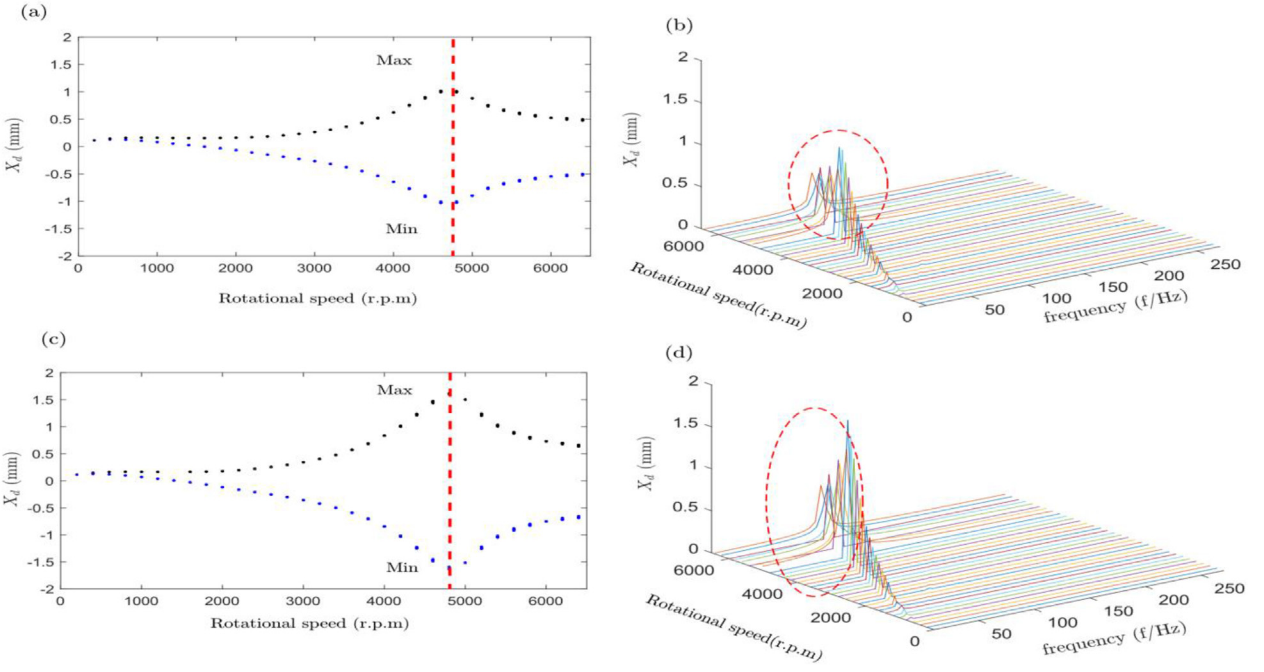

Fig. 21. Bifurcation and waterfall plots for rotor-bearing system based on nonlinear analysis at the disc location. Panels (a, c) show bifurcation diagrams, and panels (b, d) display three-dimensional spectrum diagrams for unbalanced masse 7.02×10^(-4) *kg.m and* 8.6×10^(-4) *kg.m respectively.*

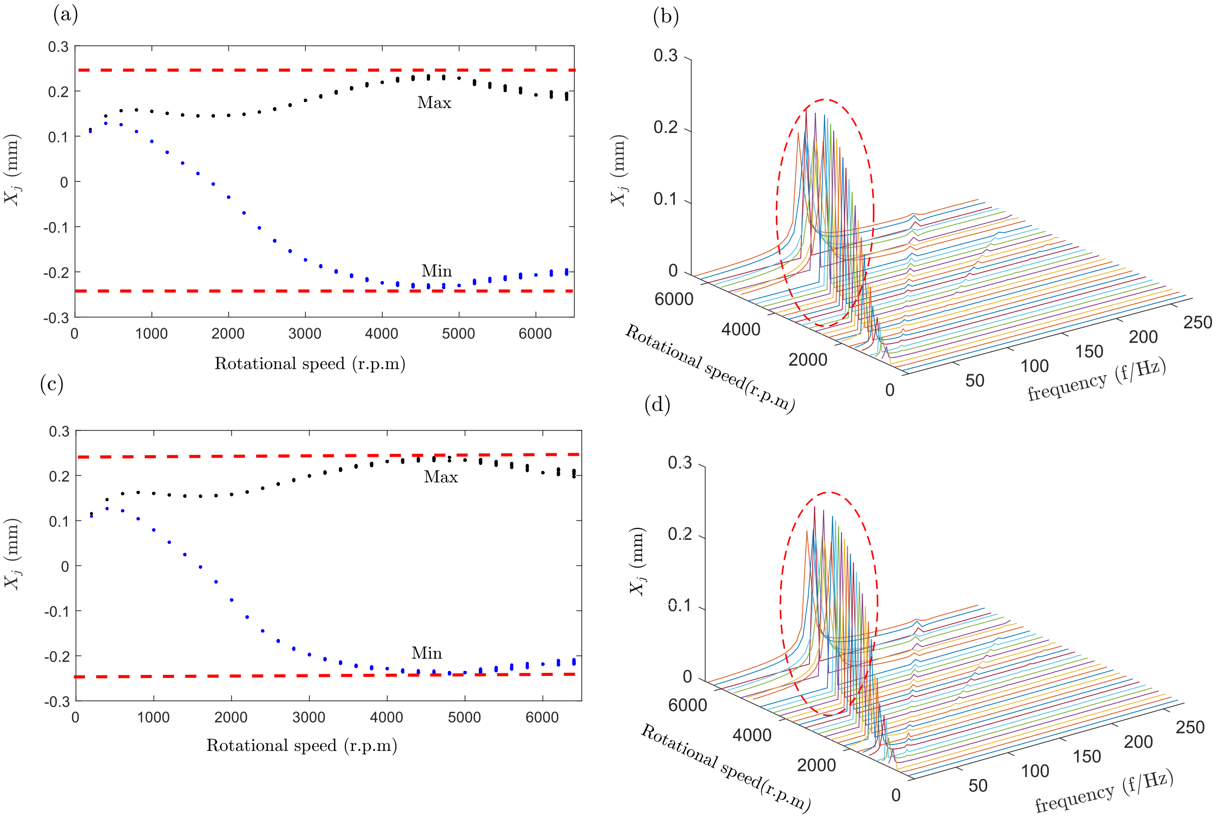

Fig. 22. Bifurcation and waterfall plots for the rotor-bearing system based on nonlinear analysis at the bearing location. Panels (a, c) illustrates bifurcation diagrams, and panels (b, d) display three-dimensional spectrum diagrams for unbalanced masses 7:02×10^-4 *kg.m and* 8:6×10^-4 *kg.m respectively.*

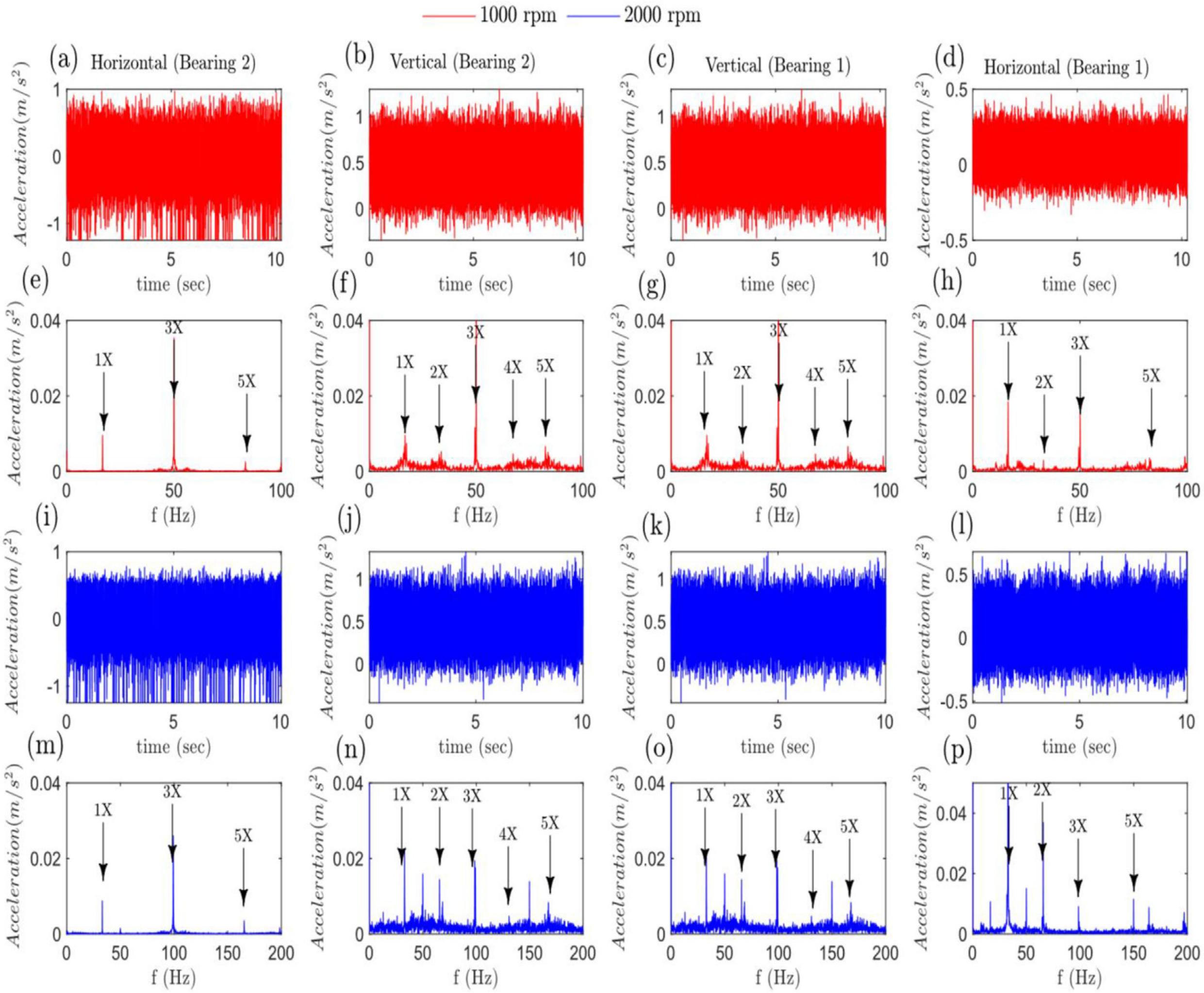

Fig. 23. Experimental results of vibration response and FFT spectrum at the horizontal and vertical directions of bearing 1 and 2 at different shaft speeds (1000, 2000 rpm). Time records in horizontal and vertical directions are shown in panels (a—d) and (i—l), while FFT spectra in horizontal and vertical directions are displayed in panels (e—h) and (m—p). FFT, fast fourier transform.

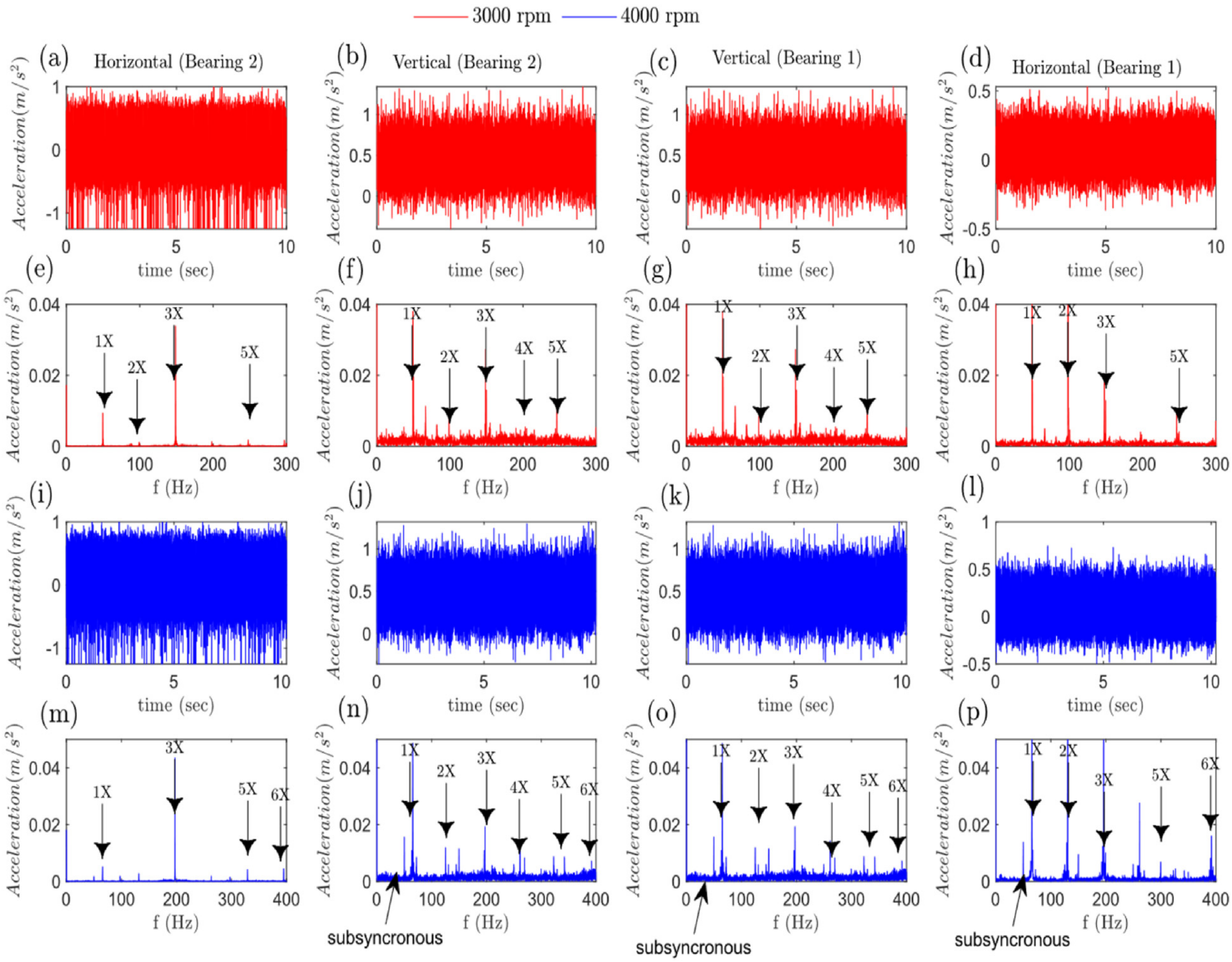

Fig. 24. Experimental results of vibration response and FFT spectrum at the horizontal and vertical directions of bearing 1 and 2 at different shaft speeds (3000, 4000 rpm). Time records in horizontal and vertical directions are shown in panels (a to d) and (i to l), while the FFT spectra in horizontal and vertical directions are displayed in panels (e to h) and (m to p). FFT, fast fourier transform.

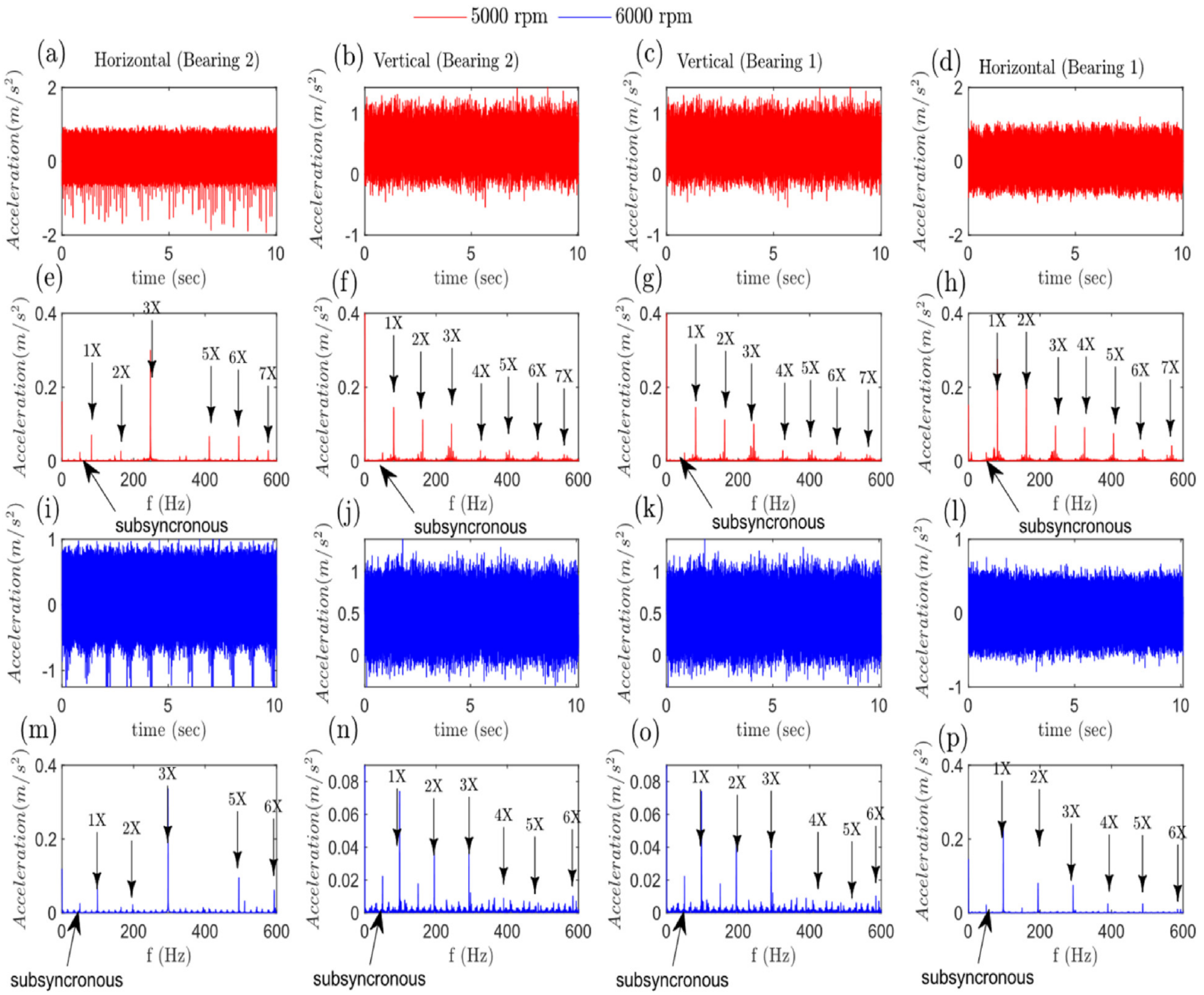

Fig. 25. Experimental results of vibration response and FFT spectrum at the horizontal and vertical directions of bearing 1 and 2 at different shaft speeds (5000–6000 rpm). Time records in horizontal and vertical directions are shown in panels (a to d) and (i to l), while FFT spectra in horizontal and vertical directions are displayed in panels (e to h) and (m to p). FFT, fast fourier transform.

and misalignment, leading to increased centrifugal forces and challenging control of the rotor-bearing system.

4. Conclusions

In this study, the nonlinear dynamic response of the rotor-bearing system is investigated using a finite-element model and validated through experimental testing. The rotor's behavior and vibration characteristics are analyzed through orbit diagrams, vibration amplitudes, time-domain responses, and FFT spectra. The study reveals the significant impact of rotational speed on the rotor-bearing system response. Below the critical speed, the system behavior remains consistent across various analyses, including first-order, second-order, nonlinear analyses, and experimental observations. However, as the speed increases, notable changes occur in the system's behavior, leading to phenomena such as whirling, whipping, and subsynchronous vibrations. These conclusion points were derived from the search results.

(1) Using linear fit polynomial equations to calculate the bearing coefficients adds a novel value by facilitating the investigation process of the rotor-bearing system behavior. This reduces the time required to calculate the bearing coefficients by 50%. See all equations in Appendix C.

(2) The theoretical model effectively assesses the rotor-bearing system's unbalance and is corroborated by experimental tests conducted

on the setup, so the stability of the rotor-bearing system is maintained at speeds below the critical speed, while instability becomes pronounced at high speeds.

(3) The theoretical and experimental analyses confirm specific resonant speeds: 5107 rpm in the theoretical analysis and 5850 rpm in the experimental analysis. Furthermore, vibration signals and FFT spectra provide insights into synchronous and subsynchronous vibration zones.

(4) The experimental test rig offers the advantage of tracking rotor orbit at any location using proximity sensors, enabling in-depth study of rotor behavior. It illustrates the oil whip phenomenon. The dynamic behavior of the rotor-bearing system is analyzed during both the acceleration and deceleration phases of shaft rotational speeds.

For future works, the author suggests the following in the area of rotor-bearing systems.

1. Experimentally analyze the behavior and dynamic characteristics of a high-speed rotor-bearing system at speeds exceeding 10 000 rpm.
2. Experimentally study the effect of applying radial load on the rotor shaft.
3. Use ANSYS in the mathematical model to study the rotor-bearing system behavior.

Funding

The authors would like to acknowledge the fund received from MYMSA Co. for manufacturing the journal bearings.

Authors contribution

OA: Conceptualization, Methodology, Formal analysis, Investigation, Writing - Original Draft.

HS: Conceptualization, Methodology, Formal analysis, Investigation, Supervision.

TE: Conceptualization, Methodology, Formal analysis, Investigation, Supervision. All authors reviewed the results and approved.

Ethics information

NA.

Data availability statement

The datasets generated during and/or analyzed during the current study are available from the corresponding author on request.

Conflicts of interest

There are no conflicts of interest.

Appendix A. Characteristics of Journal Bearings

The following Reynolds equation (Qiu and Tieu, 1995) can be solved to estimate the pressure of oil film in the journal bearing seen in Figure (A.1) panels a, b, c, and d:

$$\frac{1}{R^2}\frac{\partial}{\partial\phi}\left(\frac{\rho h^3}{12\mu}\frac{\partial p}{\partial\phi}\right)+\frac{\partial}{\partial z}\left(\frac{\rho h^3}{12\mu}\frac{\partial p}{\partial z}\right)=\frac{\Omega}{2}\frac{\partial\rho h}{\partial\phi}+\rho\frac{\partial h}{\partial t} \quad \text{(A.1)}$$

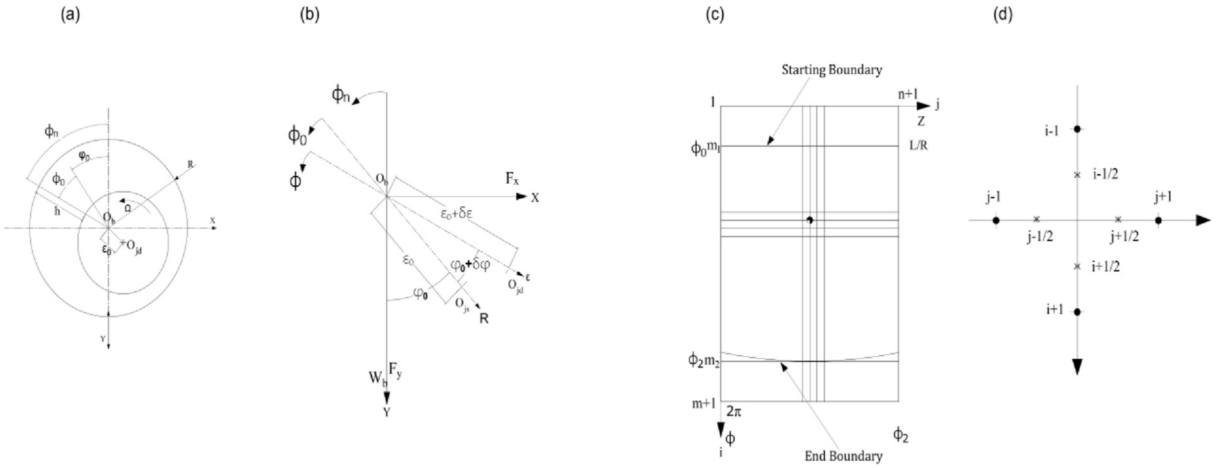

Figure A.1: Circular journal bearing: (a) journal bearing coordinates, (b) perturbed journal within a bearing, represented with angular and Cartesian coordinates, (c) oil film meshing, (d) grid points used in the half-step finite-difference method.

Here, p is the pressure of the fluid film; h is the fluid film thickness; ϕ is the angular coordinate; Ω is the rotational speed of the shaft; t is the time; and z is the axis of the shaft. The dimensionless Reynolds equation can written as follows:

$$\frac{\partial}{\partial \phi}\left(H^3\frac{\partial P}{\partial \phi}\right)+\frac{\partial}{\partial Z}\left(H^3\frac{\partial P}{\partial Z}\right)=\frac{\partial H}{\partial \phi}+2\frac{\partial H}{\partial \tau} \tag{A.2}$$

here, $H = h/c,$ c is the radial clearance, $Z = z/R$, $P = \frac{p}{6\mu\Omega}\left(\frac{c}{R}\right)^2,$ and $\tau = \Omega t$.

$$H=1+\varepsilon.cos\,(\phi_n-\varphi)=1+\varepsilon.cos\,(\phi) \tag{A.3}$$

where, $\varepsilon = c/R$, and

$$H \approx 1+(\varepsilon_0+\delta\varepsilon)\,cos(\phi_0-\delta\varphi)=1+(\varepsilon_0+\delta\varepsilon)\,[cos\,\phi_0\,cos\,\delta\varphi+sin\,\phi_0\,sin\,\delta\varphi] \tag{A.4}$$

when $\delta\varphi$ is small, $\cos(\delta\varphi) = 1-\frac{\delta\varphi^2}{2}$, and $\sin(\delta\varphi) \approx \delta\varphi$. Then,

$$\begin{aligned}H={}&H_0+\delta X.sin\,\phi_n-\delta Y.cos\,\phi_n+\frac{1}{2\varepsilon_0}\\&\left[-2\,sin\,\varphi_0\,cos\,\varphi_0\,sin\,\phi_0-sin^2\varphi_0\,cos\,\phi_0\right]\delta Y^2+\frac{1}{\varepsilon_0}\\&\left[-cos\varphi_0\,sin\,\varphi_0\,cos\,\phi_0+sin^2\varphi_0\,sin\,\phi_0\right.\\&\left.-cos^2\varphi_0\,sin\,\phi_0\right]\delta X\delta Y+\frac{1}{2\varepsilon_0}\left[2\,sin\,\varphi_0\,cos\,\varphi_0\,sin\,\phi_0\right.\\&\left.-cos^2\varphi_0\,cos\,\phi_0\right]\delta X^2=H_0+H_1+H_2+H.O.T\end{aligned} \tag{A.5}$$

where,

$$H_0=1+\varepsilon_0\,cos\,\phi_0$$

$$H_1=\delta\varepsilon\cos\phi_0+\varepsilon_0\delta\varphi\sin\phi_0$$

$$H_2=-\frac{1}{2}\delta\varepsilon\delta\varphi^2\cos\phi_0+\delta\varepsilon\delta\varphi\sin\phi_0-\frac{1}{2}\varepsilon_0\delta\varphi^2\cos\phi_0 \tag{A.6}$$

$$\begin{bmatrix}\delta X\\ \delta Y\end{bmatrix}=\begin{bmatrix}sin\,\varphi_0 & cos\,\varphi_0\\ -cos\,\varphi_0 & sin\,\varphi_0\end{bmatrix}\begin{bmatrix}\delta\varepsilon\\ \varepsilon_0\delta\varphi\end{bmatrix} \tag{A.7}$$

$$\begin{bmatrix}\delta\varepsilon\\ \varepsilon_0\delta\varphi\end{bmatrix}=\begin{bmatrix}sin\,\varphi_0 & cos\,\varphi_0\\ -cos\,\varphi_0 & sin\,\varphi_0\end{bmatrix}^{-1}\begin{bmatrix}\delta X\\ \delta Y\end{bmatrix}=\begin{bmatrix}sin\,\varphi_0 & -cos\,\varphi_0\\ cos\,\varphi_0 & sin\,\varphi_0\end{bmatrix}\begin{bmatrix}\delta X\\ \delta Y\end{bmatrix} \tag{A.8}$$

The second-order approximation of the perturbed oil layer thickness in terms of Cartesian coordinates can be expressed as follows using equations (A.7) in equation (A.8):

$$\begin{aligned}P={}&P_0+\frac{\partial P}{\partial X}\delta X+\frac{\partial P}{\partial Y}\delta Y+\frac{\partial P}{\partial X'}\delta X'+\frac{\partial P}{\partial Y'}\delta Y'+\frac{1}{2}\frac{\partial^2 P}{\partial X^2}\delta X^2\\&+\frac{1}{2}\frac{\partial^2 P}{\partial Y^2}\delta Y^2+\frac{\partial^2 P}{\partial X\partial Y}\delta X\partial Y+\frac{\partial^2 P}{\partial X'\partial X}\delta X'\partial X\\&+\frac{\partial^2 P}{\partial X'\partial Y}\delta X'\partial Y+\frac{\partial^2 P}{\partial Y'\partial X}\delta Y'\partial X+\frac{\partial^2 P}{\partial Y'\partial Y}\delta Y'\partial Y\end{aligned} \tag{A.9}$$

where (P_0) represents the steady-state pressure, the variables $X, Y, X', and\ Y'$ are defined as $\frac{x}{c}, \frac{y}{c}, \frac{x'}{\Omega c}$, and $\frac{y'}{\Omega c}$ respectively. The prime symbol ($'$) denotes the derivative with respect to τ, where $\tau = \Omega t$

To calculate the dimensionless bearing forces F_X and F_Y, the following equations are used:

$$F_X=\int_0^{\frac{L}{R}}\int_0^{2\pi}-P\,(sin\,\phi_n)d\phi_n dZ \tag{A.10}$$

$$F_Y=\int_0^{\frac{L}{R}}\int_0^{2\pi}-P\,(cos\,\phi_n)d\phi_n dZ \tag{A.11}$$

where the dimensionless bearing forces in the X and Y directions are defined as

$$\overline{F}_X=\frac{F_x}{W_b}=\frac{F_X}{\overline{W}_b} \tag{A.12}$$

$$\overline{F}_Y=\frac{F_y}{W_b}=\frac{F_Y}{\overline{W}_b} \tag{A.13}$$

where (W_b) is the bearing loa, and $\overline{W}_b = \frac{L/D}{3*\pi*S}$ as shown in Fig. 2:

$$\begin{aligned}\overline{F}_\beta={}&F_{\beta 0}+\left[\frac{\partial F_\beta}{\partial X}\delta X+\frac{\partial F_\beta}{\partial Y}\delta Y+\frac{\partial F_\beta}{\partial X'}\delta X'+\frac{\partial F_\beta}{\partial Y'}\delta Y'\right]\\&+\frac{1}{2}\left[\frac{\partial^2 F_\beta}{\partial X^2}\delta X^2+\frac{\partial^2 F_\beta}{\partial Y^2}\delta Y^2\right]+\frac{\partial^2 F_\beta}{\partial X\partial Y}\delta X\delta Y\\&+\frac{\partial^2 F_\beta}{\partial X\partial X'}\delta X\delta X'+\frac{\partial^2 F_\beta}{\partial X\partial Y'}\delta X\delta Y'+\frac{\partial^2 F_\beta}{\partial Y\partial X'}\delta Y\delta X'\\&+\frac{\partial^2 F_\beta}{\partial Y\partial Y'}\delta Y\delta Y'\end{aligned} \tag{A.14}$$

and

$$\begin{aligned}\overline{F}_{\beta} = \overline{F}_{\beta 0} &+ \left[K_{\beta X}\delta X + K_{\beta Y}\delta Y + C_{\beta X}\delta X' + C_{\beta Y}\delta Y'\right] \\ &+ \frac{1}{2}\left[K_{\beta XX}\delta X^2 + K_{\beta YY}\delta Y^2\right] + K_{\beta XY}\delta X\delta Y \\ &+ C_{\beta XX}\delta X\delta X' + C_{\beta XY}\delta X\delta Y' + C_{\beta YX}\delta Y\delta X' \\ &+ C_{\beta YY}\delta Y\delta Y'\end{aligned} \tag{A.15}$$

where $\beta = X, Y$.

The eight first-order bearing stiffness and damping coefficients can be obtained from

$$\mathrm{K}_{\mathrm{X}\beta} = \int_0^{\frac{L}{R}}\int_0^{2\pi}(-\mathrm{P}_{\beta}\,(\sin\phi_{\mathrm{n}})\mathrm{d}\phi_{\mathrm{n}}\mathrm{dZ}) \tag{A.16}$$

$$\mathrm{K}_{\mathrm{Y}\beta} = \int_0^{\frac{L}{R}}\int_0^{2\pi}(-\mathrm{P}_{\beta}(\cos\phi_{\mathrm{n}})\mathrm{d}\phi_{\mathrm{n}}\mathrm{dZ}/\overline{\mathrm{W}}_{\mathrm{b}}) \tag{A.17}$$

$$C_{X\beta} = \int_0^{\frac{L}{R}}\int_0^{2\pi}(-P_{\beta'}\,(sin\,\phi_n)d\phi_n dZ/\overline{W}_b) \tag{A.18}$$

$$C_{Y\beta} = \int_0^{\frac{L}{R}}\int_0^{2\pi}(-P_{\beta'}\,(cos\,\phi_n)d\phi_n dZ/\overline{W}_b) \tag{A.19}$$

The six second-order stiffness and eight damping bearing coefficients are

$$K_{X\beta\gamma} = \int_0^{\frac{L}{R}}\int_0^{2\pi}\left(-P_{\beta\gamma}\,(\sin\phi_n)d\phi_n dZ\big/\overline{W}_b\right) \tag{A.20}$$

$$K_{Y\beta\gamma} = \int_0^{\frac{L}{R}}\int_0^{2\pi}\left(-P_{\beta\gamma}\,(\cos\phi_n)d\phi_n dZ\big/\overline{W}_b\right) \tag{A.21}$$

$$C_{X\beta\gamma} = \int_0^{\frac{L}{R}}\int_0^{2\pi}\left(-P_{\beta\gamma'}\,(\sin\phi_n)d\phi_n dZ\big/\overline{W}_b\right) \tag{A.22}$$

$$C_{Y\beta\gamma} = \int_0^{\frac{L}{R}}\int_0^{2\pi}\left(-P_{\beta\gamma'}\,(cos\,\phi_n)d\phi_n dZ\big/\overline{W}_b\right) \tag{A.23}$$

where each of β, γ can be either X, Y.

Appendix B. Finite-Element Matrices

In this appendix, matrices representing the mass, gyroscopic effects, and stiffness of a specific mechanical system are presented. The explicit form of the mass matrix is given by the following expression:

$$[M] = \frac{\rho.A.L}{420} * \begin{bmatrix} 156 & 0 & 0 & 22l & 54 & 0 & 0 & -13l \\ 0 & 156 & -22l & 0 & 0 & 54 & 13l & 0 \\ 0 & -22l & 4l^2 & 0 & 0 & -13l & -3l^2 & 0 \\ 22l & 0 & 0 & 4l^2 & 13l & 0 & 0 & -3l^2 \\ 54 & 0 & 0 & 13l & 156 & 0 & 0 & -22l \\ 0 & 54 & -13l & 0 & 0 & 156 & 22l & 0 \\ 0 & 13l & -3l^2 & 0 & 0 & 22l & 4l^2 & 0 \\ -3l & 0 & 0 & -3l^2 & -22l & 0 & 0 & 4l^2 \end{bmatrix} \tag{B.1}$$

The matrix representing gyroscopic effects is as follows:

$$[G] = \frac{\rho.\pi.\left(\frac{d}{2}\right)^4}{120} * \begin{bmatrix} 0 & 36 & -3l & 0 & 0 & -36 & -3l & 0 \\ -36 & 0 & 0 & -3l & 36 & 0 & 0 & -3l \\ 3l & 0 & 0 & 4l^2 & -3l & 0 & 0 & -l^2 \\ 0 & 3l & -4l^2 & 0 & 0 & -3l & l^2 & 0 \\ 0 & -36 & 3l & 0 & 0 & 36 & 3l & 0 \\ 36 & 0 & 0 & 3l & -36 & 0 & 0 & 3l \\ 3l & 0 & 0 & -l^2 & -3l & 0 & 0 & 4l^2 \\ 0 & 3l & l^2 & 0 & 0 & -3l & -4l^2 & 0 \end{bmatrix} \tag{B.2}$$

Finally, the stiffness matrix is defined as

$$[K] = \frac{E.I}{L^3} * \begin{bmatrix} 12 & 0 & 0 & 6l & -12 & 0 & 0 & 6l \\ 0 & 12 & -6l & 0 & 0 & -12 & -6l & 0 \\ 0 & -6l & 4l^2 & 0 & 0 & 6l & 2l^2 & 0 \\ 6l & 0 & 0 & 4l^2 & -6l & 0 & 0 & 2l^2 \\ -12 & 0 & 0 & -6l & 12 & 0 & 0 & -6l \\ 0 & -12 & 6l & 0 & 0 & 12 & 6l & 0 \\ 0 & -6l & 2l^2 & 0 & 0 & 6l & 4l^2 & 0 \\ 6l & 0 & 0 & 2l^2 & -6l & 0 & 0 & 4l^2 \end{bmatrix} \tag{B.3}$$

Appendix C. Linear fit polynomial equations

The fitting equation for bearing coefficients in terms of eccentricity ratio:

$$\begin{aligned}\varepsilon = \Big(&1.0021 + 4.72*10^{8}\,S^{14} - 1.88*10^{9}\,S^{13}\\ &+ 3.31*10^{9}\,S^{12} - 3.43*10^{9}\,S^{11} + 2.33*10^{9}\,S^{10}\\ &- 1.088*10^{9}\,S^{9} + 3.59*10^{8}\,S^{8} - 84264000\,S^{7}\\ &+ 13914000\,S^{6} - 1564400\,S^{5} + 111340\,S^{4}\\ &- 4258.2\,S^{3} + 74.666\,S^{2} - 7.897\,S\end{aligned} \tag{C.1}$$

$$\begin{aligned}K_{xx} = \big(&1.7086 + 480040\,\varepsilon^{14} - 3144700\,\varepsilon^{13} + 9282900\,\varepsilon^{12}\\ &- 16320000\,\varepsilon^{11} + 19030000\,\varepsilon^{10} - 15513000\,\varepsilon^{9}\\ &+ 9082000\,\varepsilon^{8} - 3862900\,\varepsilon^{7} + 1194700\,\varepsilon^{6}\\ &- 266530\,\varepsilon^{5} + 42172\,\varepsilon^{4} - 4605.2\,\varepsilon^{3} + 333.82\,\varepsilon^{2}\\ &- 14.878\,\varepsilon\end{aligned} \tag{C.2}$$

$$\begin{aligned}K_{xxx} = \big(&260.59 + 143140000\,\varepsilon^{14} - 954910000\,\varepsilon^{13}\\ &+ 2.89*10^{9}\,\varepsilon^{12} - 5.19*10^{9}\,\varepsilon^{11} + 6.24*10^{9}\,\varepsilon^{10}\\ &- 5.27*10^{9}\,\varepsilon^{9} + 3.23*10^{9}\,\varepsilon^{8} - 1.5*10^{9}\,\varepsilon^{7}\\ &+ 475470000\,\varepsilon^{6} - 114140000\,\varepsilon^{5} + 19671000\,\varepsilon^{4}\\ &- 2367800\,\varepsilon^{3} + 190600\,\varepsilon^{2} - 9547\,\varepsilon\end{aligned} \tag{C.3}$$

$$\begin{aligned}C_{xx} = \big(&158.89 + 86507000\,\varepsilon^{14} - 575160000\,\varepsilon^{13}\\ &+ 1.73*10^{9}\,\varepsilon^{12} - 3.12*10^{9}\,\varepsilon^{11} + 3.72*10^{9}\,\varepsilon^{10}\\ &- 3.12*10^{9}\,\varepsilon^{9} + 1.90*10^{9}\,\varepsilon^{8} - 847080000\,\varepsilon^{7}\\ &+ 277360000\,\varepsilon^{6} - 66286000\,\varepsilon^{5} + 11386000\,\varepsilon^{4}\\ &- 1369200\,\varepsilon^{3} + 110600\,\varepsilon^{2} - 5612.2\,\varepsilon\end{aligned} \tag{C.4}$$

$$\begin{aligned}C_{xxx} = \big(&22.781 + 17098000\,\varepsilon^{14} - 109070000\,\varepsilon^{13}\\ &+ 314200000\,\varepsilon^{12} - 540890000\,\varepsilon^{11}\\ &+ 620640000\,\varepsilon^{10} - 501300000\,\varepsilon^{9} + 293370000\,\varepsilon^{8}\\ &- 126100000\,\varepsilon^{7} + 933980000\,\varepsilon^{6} - 9234000\,\varepsilon^{5}\\ &+ 1534800\,\varepsilon^{4} - 177970\,\varepsilon^{3} + 13758\,\varepsilon^{2} - 658.59\,\varepsilon\end{aligned} \tag{C.5}$$

Appendix D. Dimensional stiffness and damping coefficients for ungrooved journal bearing versus the rotational speed

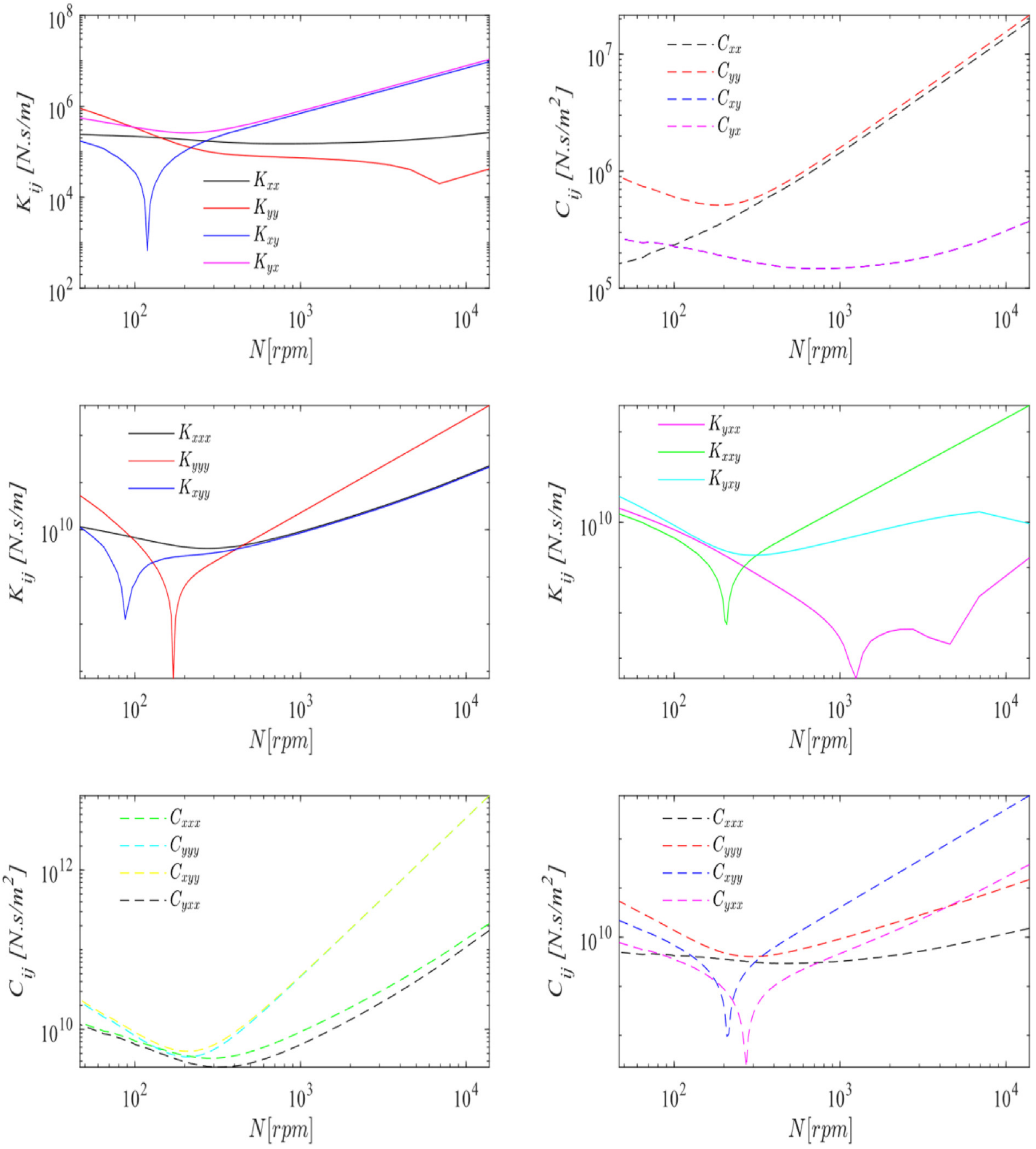

Figure D.1: (Color online) Log-log plot for ungrooved journal bearing dimensional stiffness and damping coefficients versus the rotational speed. The figure included first-order bearing coefficients and second-order bearing coefficients at $L/D = 2.5$*. In this figure, the mesh size is 100 × 400.*

References

Adiletta, G., Guido, A. R., & Rossi, C. (1997). Nonlinear dynamics of a rigid unbalanced rotor in journal bearings. Part II: experimental analysis. *Nonlinear Dynamics, 14*, 157–189.

Ahmed, O., El-Sayed, T., & Sayed, H. (2023). Finite element analyses of rotor/bearing system using second-order journal bearings stiffness and damping coefficients. *Journal of Vibration and Control, 0*, Article 10775463231204388.

Al Yahyai, M., & Mba, D. (2014). Rotor dynamic response of a centrifugal compressor due to liquid carry over: a case study. *Engineering Failure Analysis, 45*, 436–448.

Baddour, N. (2008). Hamilton's principle for the derivation of equations of motion. In M. Alvarez (Ed.), *Leading-Edge Applied*

Mathematical Modeling Research (pp. 155–182). New York, NY, USA: Nova Science Publisher.

Balducchi, F., Arghir, M., & Gauthier, R. (2015). Experimental analysis of the unbalance response of rigid rotors supported on aerodynamic foil bearings. *Journal of Vibration and Acoustics, 137*.

Braut, S., Žigulić, R., & Butković, M. (2008). Numerical and experimental analysis of a shaft bow influence on a rotor to stator contact dynamics. *Journal of Mechanical Engineering, 54*, 693–706.

Briend, Y., Chatelet, E., Dufour, R., Andrianoely, M.-A., Legrand, F., & Baudin, S. (2021). Dynamics of on-board rotors on finite-length journal bearings subject to multi-axial and multi-frequency excitations: numerical and experimental investigations. *Mécanique & Industries, 22*, 35.

De Rosa, E., & Rossi, C. (1996). Dynamic behavior of an unbalanced rotor on lubricated bearings. *Tribology Transactions, 39*, 859–869.

Driot, N., Lamarque, C. H., & Berlioz, A. (2006). *Theoretical and experimental analysis of a base-excited rotor* (pp. 257–263).

El-Sayed, T., & Farghaly, S. (2016). Exact free vibration analysis of Timoshenko stepped shaft carrying elastically supported eccentric masses with application on SWRO mechanical system. *Desalination, 385*, 194–206.

El-Sayed, T. A., & Fatah, A. A. A. (2016). Performance of hydraulic turbocharger integrated with hydraulic energy management in SWRO desalination plants. *Desalination, 379*, 85–92.

El-Sayed, T., & Sayed, H. (2022). Bifurcation analysis of rotor/ bearing system using third-order journal bearing stiffness and damping coefficients. *Nonlinear Dynamics, 107*, 123–151.

El-Sayed, T., Friswell, M. I., & Sayed, H. (2023). Approximating fluid bearing characteristics using polynomials for the nonlinear dynamics of rotating machines. *Tribology International, 187*, Article 108669.

Elsayed, E. K., Sayed, H., & El-Sayed, T. (2023). Analysis of Second-Order Thrust Bearing Coefficients Considering Misalignment Effect. *Journal of Vibration Engineering & Technologies, 12*(2), 1957–1977.

Flack, R., & Rooke, J. (1980). A theoretical-experimental comparison of the synchronous response of a bowed rotor in five different sets of fluid film bearings. *Journal of Sound and Vibration, 73*, 505–517.

Gupta, K., Gupta, K., & Athre, K. (1993). Unbalance response of a dual rotor system: theory and experiment. *Journal of Vibration and Acoustics, 115*(4), 427–435.

Hamdoon, F. O., Al-Bugharbee, H. R., & Hameed, A. S. (2012). Transient response of rotor system under different startup speed profiles. *Education, 2015*.

Hashimoto, H., & Wada, S. (1990). *Dynamic behavior of unbalanced rigid shaft supported on turbulent journal bearings—theory and experiment* (pp. 404–408).

Huang, G., Wang, X., Qin, X., Zhu, L., & Yi, S. (2022). Experimental investigation of dynamic behavior of rotor system with a novel double layers flexible support tilting pad bearing. *Advances in Mechanical Engineering, 14*, Article 16878132221116482.

Jalali, M. H., Ghayour, M., Ziaei-Rad, S., & Shahriari, B. (2014). Dynamic analysis of a high speed rotor-bearing system. *Measurement, 53*, 1–9.

Kartheek, A., Vijayan, K., Sun, X., & Marburg, S. (2023). Stochastic analysis of flexible rotor supported on hydrodynamic bearings. *Mechanical Systems and Signal Processing, 203*, Article 110699.

Katinić, M., Kolar, J., Konjatić, P., & Bošnjaković, M. (2023). Unbalance response analysis of a rotor kit with two identical discs located between bearings. *Tehnički Glasnik, 17*, 324–331.

Kreuzinger-Janik, T., & Irretier, H. (2000). Experimental modal analysis—a tool for unbalance identification of rotating machines. *International Journal of Rotating Machinery, 6*, 11–18.

Laha, S. K. (2010). *Analysis of stability and unbalance response of flexible rotor supported on hydrodynamic porous journal bearing*. Indian Institute of Technology Guwahati. PhD Thesis.

Lee, J., & Van Moorhem, W. (1996). *Analytical and experimental analysis of a self-compensating dynamic balancer in a rotating mechanism* (pp. 468–475).

Li, Y., Luo, Z., Liu, J., Ma, H., & Yang, D. (2021). Dynamic modeling and stability analysis of a rotor-bearing system with bolted-disk joint. *Mechanical Systems and Signal Processing, 158*, Article 107778.

Lu, H., Li, W., Shen, J., Chen, T., & Sheng, L. (2024). Dynamic characteristics analysis of rotor-bearing system considering bearing clearance and hybrid eccentricity. *Journal of Vibration Engineering & Technologies, 12*, 2249–2263.

Meybodi, R. R., Mohammadi, A. K., & Bakhtiari-Nejad, F. (2012). Numerical analysis of a rigid rotor supported by aerodynamic four-lobe journal bearing system with mass unbalance. *Communications in Nonlinear Science and Numerical Simulation, 17*, 454–471.

Miraskari, M., Hemmati, F., & Gadala, M. S. (2018a). Nonlinear dynamics of flexible rotors supported on journal bearings—Part I: Analytical bearing model. *Journal of Tribology, 140*, Article 021704.

Miraskari, M., Hemmati, F., & Gadala, M. S. (2018b). Nonlinear dynamics of flexible rotors supported on journal bearings—part II: numerical bearing model. *Journal of Tribology, 140*, Article 021705.

Mourelatos, Z. P. (2001). An efficient journal bearing lubrication analysis for engine crankshafts. *Tribology Transactions, 44*, 351–358.

Mutra, R. R., & Srinivas, J. (2020). Dynamic analysis of a turbocharger rotor-bearing system in transient operating regimes. *J Inst Eng (India) Series C, 101*, 771–783.

Mutra, R. R., & Srinivas, J. (2021). Parametric design of turbocharger rotor system under exhaust emission loads via surrogate model. *Journal of the Brazilian Society of Mechanical Sciences and Engineering, 43*, 117.

Mutra, R. R., & Srinivas, J. (2022). An optimization-based identification study of cylindrical floating ring journal bearing system in automotive turbochargers. *Meccanica, 57*, 1193–1211.

Özer, A., Ghodsi, M., Sekiguchi, A., Saleem, A., & Al-Sabari, M. N. (2015). Design and experimental implementation of a beam-type twin dynamic vibration absorber for a cantilevered flexible structure carrying an unbalanced rotor: numerical and experimental observations. *Shock and Vibration, 2015*(1), 154892.

Parmar, V., Saran, V. H., & Harsha, S. (2020). Effect of an unbalanced rotor on dynamic characteristics of double-row self-aligning ball bearing. *European Journal of Mechanics - A: Solids, 82*, Article 104006.

Perez, N., & Rodríguez, C. (2021). Vertical rotor model with hydrodynamic journal bearings. *Engineering Failure Analysis, 119*, Article 104964.

Qiu, Z., & Tieu, A. (1995). *Misalignment effect on the static and dynamic characteristics of hydrodynamic journal bearings* (pp. 717–723).

Rao, S. S., & Yap, F. F. (1995). *Mechanical vibrations* (vol. 4). New York: Addison-Wesley.

San Andrés, L. (2006). Introduction to pump rotordynamics. *Design Analy High Speed Pumps, 9*, 1–26.

Sayed, H., & El-Sayed, T. (2022a). Nonlinear dynamics and bifurcation analysis of journal bearings based on second order stiffness and damping coefficients. *International Journal of Non-Linear Mechanics, 142*, Article 103972.

Sayed, H., & El-Sayed, T. (2022b). A novel method to evaluate the journal bearing forces with application to flexible rotor model. *Tribology International, 173*, Article 107593.

Sayed, Hussein, El-Sayed, Tamer A., & Friswell, M. I. (2023). Continuation analysis of rotor bearing systems through direct solution of reynolds equation. In *Advances in Transdisciplinary Engineering*.

Scheffer, C., & Girdhar, P. (2004). *Practical machinery vibration analysis and predictive maintenance*. UK: Elsevier.

Shen, X., Jia, J., Zhao, M., & Jing, J. (2008). Numerical and experimental analysis of the rotor—bearing—seal system. *Journal of Mechanical Engineering and Sciences, 222*, 1435–1441.

Sinha, J. K., Lees, A., & Friswell, M. (2004). Estimating unbalance and misalignment of a flexible rotating machine from a single run-down. *Journal of Sound and Vibration, 272*, 967–989.

Taplak, H., & Parlak, M. (2012). Evaluation of gas turbine rotor dynamic analysis using the finite element method. *Measurement, 45*, 1089–1097.

Tofighi-Niaki, E., & Safizadeh, M. S. (2023). Dynamic of a flexible rotor-bearing system supported by worn tilting journal bearings experiencing rub-impact. *Lubricants, 11*, 212.

Wang, J., & Khonsari, M. (2006). On the hysteresis phenomenon associated with instability of rotor-bearing systems. *Journal of Tribology, 128*(1), 188–196.

Wang, L., Wang, A., Yin, Y., Heng, X., & Jin, M. (2022). Effects of unbalance orientation on the dynamic characteristics of a double overhung rotor system for high-speed turbochargers. *Nonlinear Dynamics, 107*, 665–681.

Xu, M., & Marangoni, R. (1994). Vibration analysis of a motor-flexible coupling-rotor system subject to misalignment and unbalance, part I: theoretical model and analysis. *Journal of Sound and Vibration, 176*, 663–679.

Yin, T., Zhang, G., Du, J., & To, S. (2021). Nonlinear analysis of stability and rotational accuracy of an unbalanced rotor supported by aerostatic journal bearings. *IEEE Access, 9*, 61887–61900.

Zanarini, A., & Cavallini, A. (2012). Experiencing rotor and fluid film bearing dynamics. *Proc Quinta Giornata di Studio Ettore Funaioli*, 23–38.

Zhang, J., Kang, W., & Liu, Y. (2009). *Numerical method and bifurcation analysis of Jeffcott rotor system supported in gas journal bearings* (p. 011007).

Zhao, J., Linnett, I., & McLean, L. (1994). *Stability and bifurcation of unbalanced response of a squeeze film damped flexible rotor* (pp. 361–368).

Zhu, H. M., Chen, W. F., Zhu, R. P., Zhang, L., Gao, J., & Liao, M. J. (2020). Dynamic analysis of a flexible rotor supported by ball bearings with damping rings based on FEM and lumped mass theory. *J Centr South Univ, 27*, 3684–3701.